, , pp. 1–21

doi:

Spartan: Spatial Activation Aware Transcriptomic Analysis Network

Mohammad Faiz Iqbal Faiz,[1] Elliot Jokl,[2] Rachel Jennings,[2] Karen Piper Hanley,[2] Andrew Sharrocks,[3] Mudassar Iqbal[1]* and Syed Murtuza Baker[1]*

[1]Division of Informatics, Imaging & Data Sciences, School of Health Sciences, University of Manchester, Oxford Road, M13 9PL, Manchester, United Kingdom, [2]Division of Diabetes, Endocrinology & Gastroenterology, School of Medical Sciences, University of Manchester, Oxford Road, M13 9PL, Manchester, United Kingdom and [3]Division of Molecular & Cellular Function, School of Biological Sciences, University of Manchester, Oxford Road, M13 9PL, Manchester, United Kingdom

*Corresponding authors. syed.murtuzabaker@manchester.ac.uk, mudassar.iqbal@manchester.ac.uk

Spatial transcriptomics is rapidly advancing toward single cell level resolution, revealing complex tissue architectures organized across continuous anatomical gradients. However, accurate identification of spatial domains remains a central computational challenge, as many existing clustering approaches blur anatomical boundaries, merge transitional zones, or fail to resolve localized microstructures. Here we introduce Spartan, an activation-aware multiplex graph framework that explicitly models spatial transitions for high-resolution domain discovery. Spartan integrates spatial topology, Local Spatial Activation (LSA), a neighborhood deviation signal that amplifies localized transcriptomic shifts often attenuated by similarity-based clustering. By jointly modeling cohesion within domains and activation at interfaces, Spartan recovers anatomically aligned partitions across spatially resolved transcriptomics technologies including Visium HD, MERFISH, Stereo-seq, and STARmap. We demonstrate its utility in a high-resolution Visium HD section of developing human esophagus and stomach, where activation-aware graph integration enables precise delineation of transitional regions such as the gastroesophageal junction and supports stable multi-scale domain recovery without fragile hyperparameter tuning. Beyond domain identification, Spartan leverages activation-aware structure to detect spatially variable genes associated with localized tissue remodeling. Spartan scales near-linearly with dataset size, providing a robust and interpretable framework for spatial systems-level analysis.

Key words: Spatial transcriptomics, Spatial domains, Spatially variable genes, Local spatial autocorrelation

Introduction

Spatially resolved transcriptomics (SRT) enables gene expression to be measured directly in intact tissue, allowing molecular states to be mapped onto anatomical structures [1, 2, 3]. As SRT technologies increase in resolution and scale, datasets now contain tens of thousands of spatial locations exhibiting fine-grained transcriptional heterogeneity [4]. Accurately resolving spatial organization within such data remains a central computational challenge. A core task in SRT analysis is spatial domain identification, in which spatial locations are grouped into coherent regions with shared transcriptional programs. Most existing approaches integrate spatial proximity with gene expression similarity to infer such domains, which effectively separates major tissue compartments. However, complex tissues frequently contain localized microenvironments embedded within broader regions, including boundary-adjacent zones and niche-like structures, where subtle transcriptional shifts define functional specialization. Under these conditions, similarity-driven clustering can blur interfaces, merge anatomically distinct regions, and overlook fine microstructures that are biologically meaningful.

To better capture this fine-scale organization, we reasoned that spatial domain discovery should measure not only what each cell or spot expresses and where it resides, but also how its molecular state differs from its immediate neighborhood. We introduce this third signal as Local Spatial Activation (LSA), a quantitative measure of deviation from surrounding transcriptional context in a low-dimensional latent space. Intuitively, LSA highlights regions where transcriptional programs shift locally, including tissue interfaces, remodeling fronts, and nested microstructures. Unlike conventional similarity-driven graph constructions that primarily reinforce local homogeneity, LSA explicitly models deviation from neighborhood context, allowing spatial transitions to actively shape domain boundaries rather than being smoothed away. Although conceptually related to local spatial statistics such as Moran's I [5, 6], LSA is formulated to operate directly on transcriptomic representations and to emphasize activation at spatial transitions (Fig. 1).

Motivated by this principle, we developed Spartan (Spatial Activation Aware Transcriptomic Analysis Network), a framework for spatial domain recovery that integrates three complementary layers within an aggregated graph: spatial

© The Author . Published by Oxford University Press. All rights reserved. For permissions, please e-mail: journals.permissions@oup.com

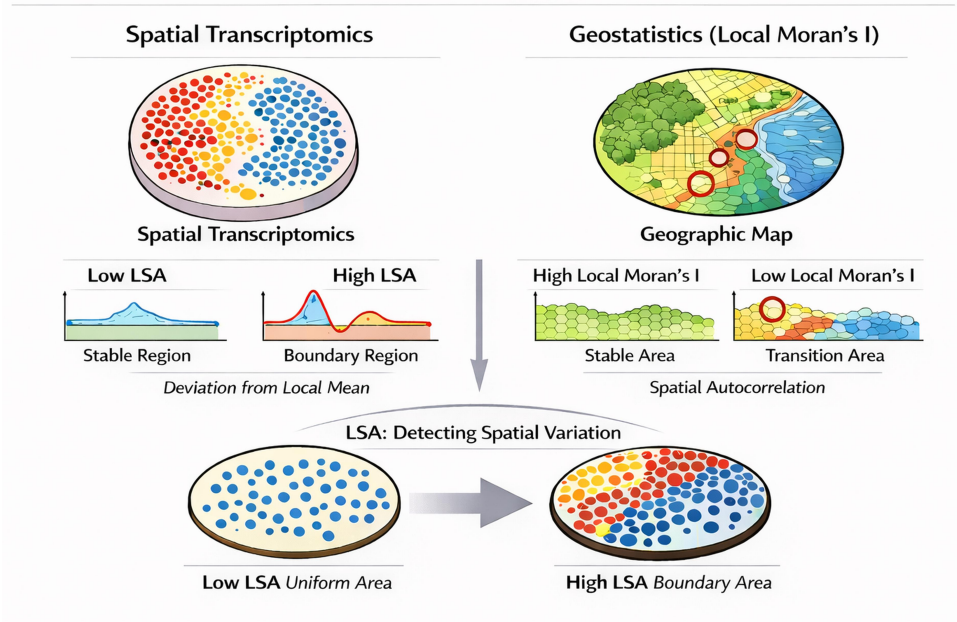

Figure 1. Local Spatial Activation (LSA) highlights tissue interfaces and local transcriptional transitions. Schematic illustration comparing Spartan's LSA with local Moran's I (a local indicator of spatial association; LISA) from geostatistics. LSA is low within spatially stable domains where neighboring spots share similar transcriptional states, but increases at boundaries and transition regions where molecular profiles deviate from the local neighborhood. In contrast, local Moran's I is high in homogeneous regions with strong local autocorrelation and decreases across transition zones. Together, the figure links Spartan's activation-based view of spatial variation to classical spatial statistics concepts, explaining how LSA supports sharper boundary fidelity and improved spatial domain resolution in complex tissues.

topology, LSA, and gene expression connectivity. Unlike existing spatial clustering approaches that encode spatial proximity and expression similarity within a single homogeneous graph layer, Spartan introduces deviation-based activation as an explicit structural component of the clustering objective. Spartan applies Leiden community detection [7] to this activation-aware graph, enabling efficient and reproducible domain identification while preserving interpretability through explicit layer weighting and transparent parameterization. By encoding activation as an explicit graph layer, Spartan enables boundary-sensitive clustering while maintaining stable multi-scale behavior across datasets. The aggregated formulation allows Spartan to adapt between datasets dominated by broad compartmental structure and those requiring sensitivity to fine local heterogeneity.

In high-resolution samples, such as Visium HD sections of the developing human esophagus and stomach, biologically meaningful organization is expressed as thin layers, curved anatomical boundaries, and junctional transition zones, including the gastroesophageal junction (GEJ), where epithelial and stromal programs change gradually rather than forming sharply separated compartments. Resolving such continuous spatial organization illustrates the type of challenge that activation-aware graph integration is designed to address.

We benchmarked Spartan across multiple SRT technologies, including MERFISH, Stereo-seq, STARmap, and osmFISH, spanning diverse resolutions and tissue architectures. Spartan achieved strong and consistent performance across datasets, frequently matching or exceeding recently proposed methods including BANKSY [8], NichePCA [9], and SpatialLeiden [10]. Ablation analyses confirmed the complementary contribution of each graph component, with the multiplex configuration providing the most robust domain recovery across technologies and experimental settings. Beyond spatial domain identification, Spartan extends naturally to spatially variable gene detection by leveraging LSA to identify genes associated with localized spatial patterning, providing a scalable and extensible framework for spatial transcriptomics and future spatial multi-omics integration.

Results

Overview of Spartan

Spartan is a computational framework for the accurate identification of spatial domains and detection of spatially variable genes (SVGs) across diverse SRT platforms. It integrates spatial topology and gene expression structure through three complementary and biologically grounded graphs that jointly encode spatial proximity, LSA, and expression similarity.

From each SRT sample, Spartan extracts spatial coordinates and a preprocessed count matrix $\mathbf{X}$, performs principal-component analysis to obtain $\mathbf{Y}^{pca}$, and constructs three complementary graphs (Fig. 2A). The spatial graph, represented by adjacency matrix $\mathbf{S}$ (Fig. 2B), encodes physical neighborhood relationships between spots using either k-nearest-neighbor (KNN) or Delaunay connectivity. A central component of Spartan is the LSA graph, represented by $\mathbf{L}$ (Fig. 2C). For each pair of neighboring spots i and j, the weight l_{ij} combines their attribute deviations ϕ_i and ϕ_j with a spatial proximity term w^r_{ij}. This formulation quantifies LSA, providing an additional spatial signal that distinguishes structured spatial variation from random expression noise. The gene expression connectivity graph, represented by adjacency matrix $\mathbf{G}$ (Fig. 2D), captures transcriptomic similarity in the PCA-reduced space.

Spartan integrates these three graphs into an aggregated graph, represented by the weighted adjacency matrix $\mathbf{J}$

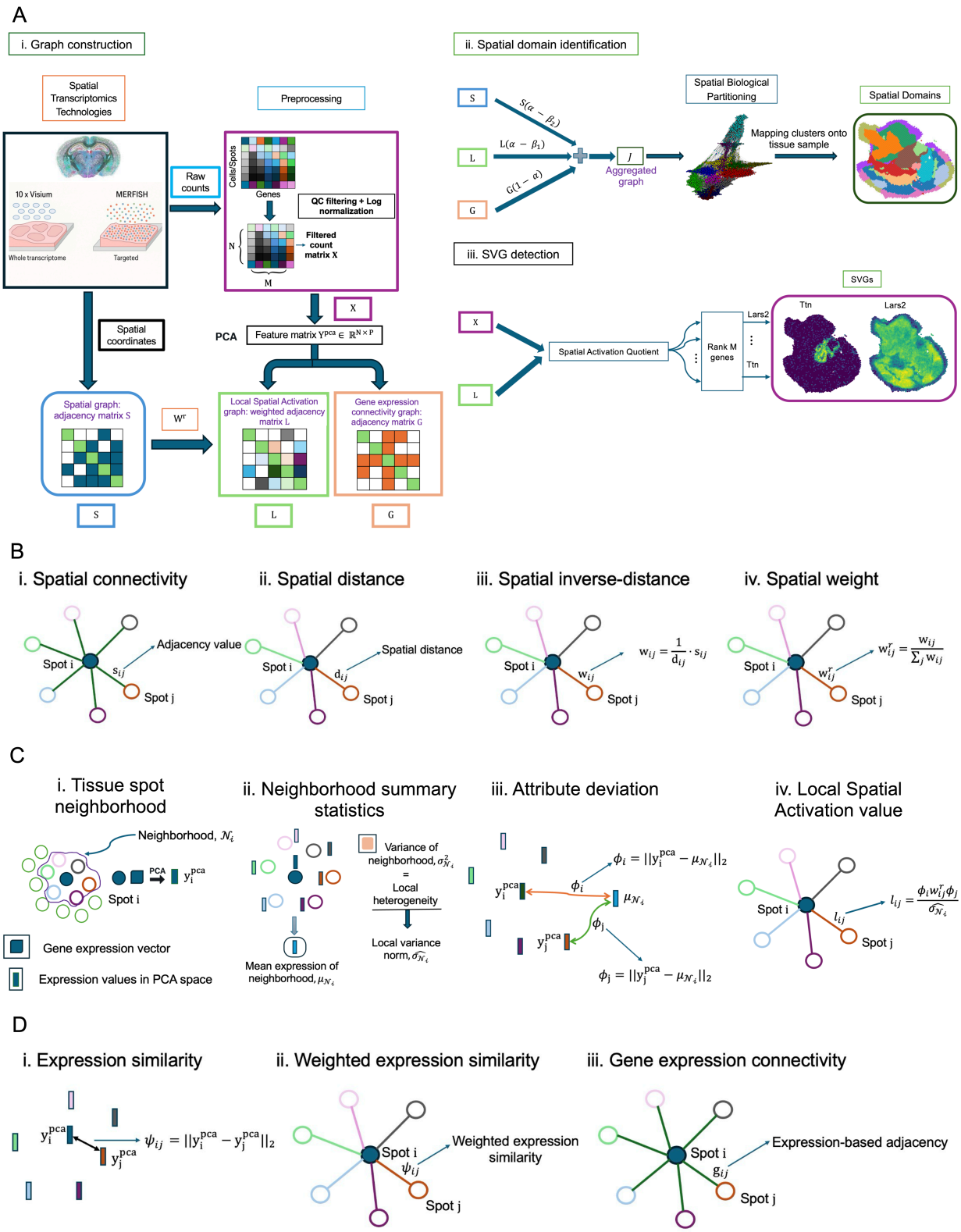

Figure 2. Overview of Spartan Spartan identifies spatial domains and spatially variable genes (SVGs) through multiplex integration of spatial and transcriptomic information. (A) Spartan extracts the raw count matrix to get filtered count matrix $\mathbf{X}$, performs PCA to obtain $\mathbf{Y^{pca}}$, and constructs three complementary graphs: a spatial graph encoding spot proximity, a Local Spatial Activation (LSA) graph capturing fine-scale spatial dependencies that provide unique biological signals, and a gene-expression similarity graph capturing transcriptomic relationships. These graphs are integrated into an aggregated graph (represented by weighted adjacency matrix $\mathbf{J}$), where Leiden clustering yields biologically coherent spatial domains. The Spatial Activation Quotient (SAQ), derived from the LSA graph, ranks genes by their local activation strength to identify SVGs. (B) The spatial graph's adjacency matrix $\mathbf{S}$ is formed using spatial connectivity and used to construct row-normalized spatial weights matrix $\mathbf{W^r}$. (C) The LSA graph adjacency $\mathbf{L}$ combines spatial proximity and attribute similarity. (D) The gene expression connectivity graph (represented by adjacency matrix $\mathbf{G}$) encodes neighborhood relationships in the PCA-reduced space.

(Fig. 2A) that balances spatial continuity and gene expression similarity. Leiden clustering on $\mathbf{J}$ partitions the tissue into coherent spatial domains that align with known anatomical regions. To further exploit the LSA signal, Spartan computes a Spatial Activation Quotient (SAQ) (Fig. 2A) for each gene by combining $\mathbf{L}$ and $\mathbf{X}$, ranking genes by their spatial activation strength to identify SVGs.

By modeling spatial relationships at multiple levels, including global proximity ($\mathbf{S}$), LSA ($\mathbf{L}$), and transcriptomic similarity ($\mathbf{G}$), Spartan reveals biologically coherent tissue organization and spatially patterned gene programs. Its independence from specific SRT technologies and its ability to detect both structured domains and fine-grained local patterns make Spartan a general and extensible framework for spatial omics analysis.

Ablation study of multiplex graph components

Next, we conducted an ablation study to evaluate the contribution of each component in the aggregated graph gr^{mul}. The aggregated graph comprises three elements (Equation 14): (i) the LSA graph gr^{lsa}, represented by the weighted adjacency matrix $\mathbf{L}$, (ii) the gene expression connectivity graph gr^{g}, represented by $\mathbf{G}$, and (iii) the spatial graph gr^{s}, represented by $\mathbf{S}$. We considered three combinations of these graphs that have both structural and expression-based terms: (i) $\mathbf{L}+\mathbf{S}+\mathbf{G}$, (ii) $\mathbf{L}+\mathbf{G}$, and (iii) $\mathbf{S}+\mathbf{G}$. For dual-graph formulations ($\mathbf{L}+\mathbf{G}$ or $\mathbf{S}+\mathbf{G}$), the combined adjacency matrix was defined as $\alpha \cdot (\mathbf{L} \text{ or } \mathbf{S}) + (1-\alpha) \cdot \mathbf{G}$. The β_1 and β_2 parameters were only used in $\mathbf{L}+\mathbf{S}+\mathbf{G}$ configurations. Each combination was further subdivided by neighborhood connectivity type, either k-nearest neighbors (KNN) graph or Delaunay triangulation, resulting in six configurations in total. These configurations were evaluated across four datasets representing different SRT technologies. For multi-sample datasets, the multiplex weighting parameter α was selected using a cross-sample hierarchical strategy to avoid sample-specific overfitting (α-selection strategy).

We evaluated all configurations across multiple datasets using the R score and ARI score (Fig. 3A-B). Overall, the ablation study supports the aggregated graph formulation implemented in Spartan. Across eight SRT samples from different technologies, including MERFISH and STARmap, the multiplex configuration ($\mathbf{L}+\mathbf{S}+\mathbf{G}$) consistently performed well across all samples. Specifically, the aggregated graph using KNN-based spatial connectivity ranked best in two samples and second best in five, demonstrating strong generalization across datasets. The Delaunay-based configuration also performed competitively, ranking best in one sample, although KNN-based connectivity offers greater stability across all datasets. In contrast, the dual-graph configurations ($\mathbf{L}+\mathbf{G}$ or $\mathbf{S}+\mathbf{G}$) exhibited greater variability across samples and technologies. Notably, these dual configurations displayed an inverse relationship: when $\mathbf{L}+\mathbf{G}$ achieved high performance, $\mathbf{S}+\mathbf{G}$ tended to perform poorly, and vice versa. Together, these findings demonstrate that the individual components of Spartan's aggregated graph—the LSA graph, spatial graph, and gene expression connectivity graph—contribute complementary spatial and transcriptomic information, leading to more stable and biologically coherent clustering outcomes across diverse SRT datasets.

Spartan reveals biologically coherent domains in the mouse E9.5 embryo

The Spartan clustering results on the E9.5E2S2 sample demonstrate its strong effectiveness in identifying biologically meaningful domains (Fig. 3C). Visually, Spartan generates continuous spatial domains without fragmentation, which aligns well with the tissue morphology. This suggests that Spartan's graph construction strategy, which leverages LSA in addition to expression similarity, is well-suited for early embryo tissue where spatial gradients and sharp regional boundaries coexist.

The contingency table (ground truth vs. predicted clusters) (Fig. 3D) provides a quantitative view of Spartan's mapping accuracy. Most tissues, such as the spinal cord, surface ectoderm, heart, and liver, map cleanly to unique predicted clusters, visible as strong diagonal blocks. The predicted clusters broadly recapitulate the major anatomical compartments annotated [11]: forebrain, heart, liver, spinal cord, mesenchyme, and others (Supplementary Fig. 1A). Some tissues, such as mesenchyme and head mesenchyme, exhibit partial overlap across multiple predicted clusters. This is not necessarily an error: mesenchyme is known to be heterogeneous and spread across numerous anatomical regions in E9.5 embryos [11], so splitting into multiple clusters may reflect biological heterogeneity or annotation granularity rather than misclassifications. Thus, Spartan not only recovers the ground truth domains but also reveals finer granularity potentially providing new biological insights.

Overall, these results highlight Spartan's effectiveness not just in matching ground truth but in extending beyond it by resolving complex tissues into subdomains.

Spartan achieves top-tier performance on public SRT datasets

The benchmarking study was divided into two parts. First, Spartan was benchmarked against representative and widely used methods for spatial domain identification using datasets from the SDMBench suite of datasets. Second, Spartan was compared against recently proposed methods using multiple datasets, including those from the SDMBench as well as the Vizgen MERFISH dataset. Two versions of Spartan were evaluated: Spartan (v1), which employs a Delaunay graph to represent neighborhood connectivity in spatial coordinate space, and Spartan (v2), which employs a KNN graph to represent neighborhood relations.

Benchmarking on SDMBench

Spartan was benchmarked on six datasets from the SDMBench: STARmap, STARmap*, MERFISH, BaristaSeq, osmFISH, and Stereo-seq (Datasets). For competing methods, we report the published SDMBench results [12] to ensure direct comparability under a standardized benchmarking framework. Spartan was evaluated using the same preprocessing strategy (HVG selection, PCA dimensionality, neighborhood construction) and with the number of predicted clusters matched to the ground-truth domain count, consistent with prior studies [9, 10]. Performance was assessed in comparison with five representative and widely used methods: BASS [13], GraphST [14], SpaGCN [15], SCAN-IT [16] and SpaceFlow [17], as well as the standard Leiden clustering algorithm.

For both multi-sample and single-sample datasets, we deployed the hierarchical α-selection strategy to obtain the optimal α_{best} as described in sections α-selection strategy and Ablation study of multiplex graph components. In single-sample

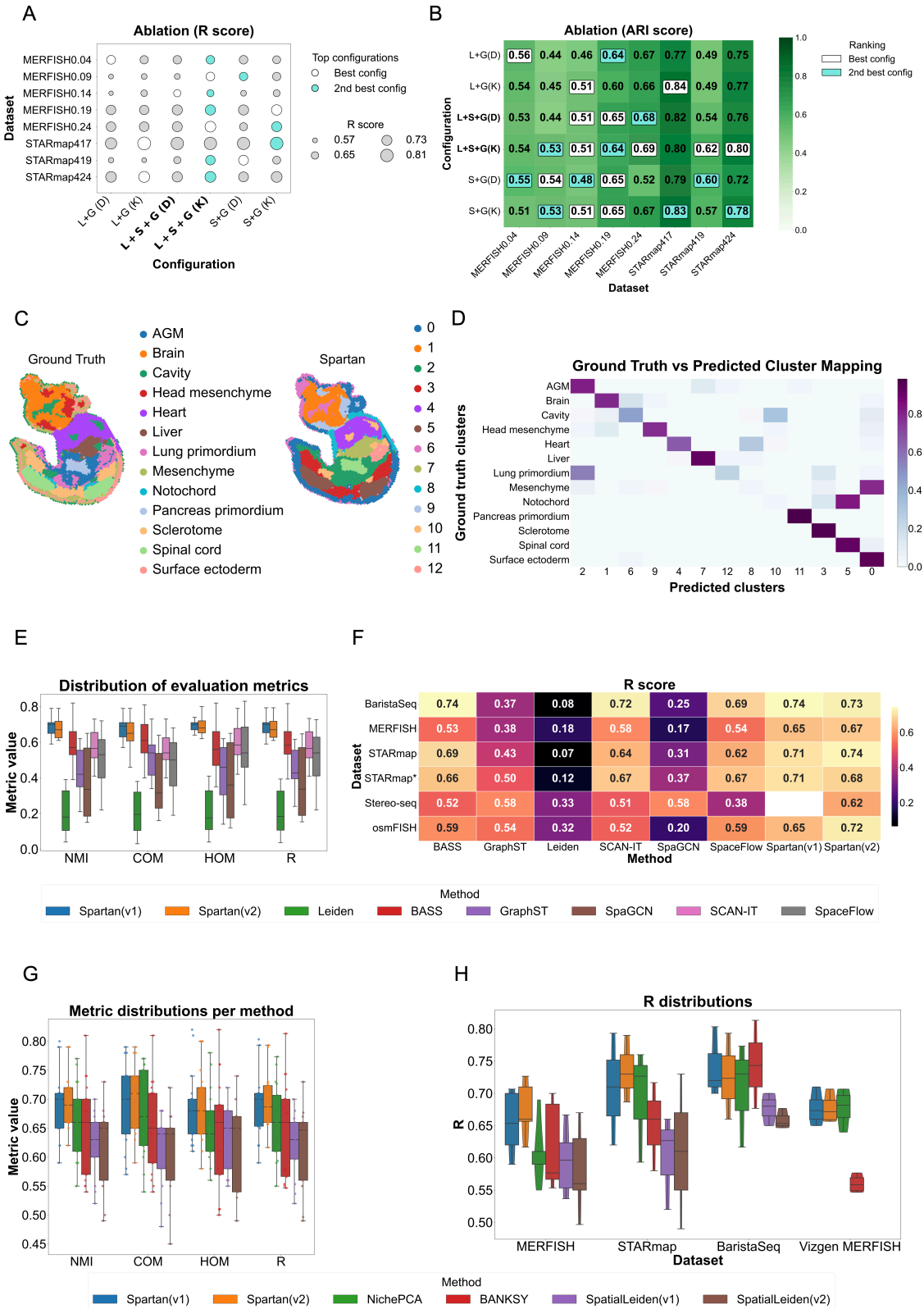

Figure 3. (A–B) Graph ablation. (A) R scores for combinations of LSA (**L**), spatial (**S**), and gene expression connectivity (**G**) graphs using KNN (K) or Delaunay (D) neighborhoods; circle size denotes R, colors indicate best and second-best configurations. (B) Dataset-wise ablation confirms the contribution of each graph component. (C–D) Spatial reconstruction. (C) Example Stereo-seq sample showing ground-truth anatomy (left) and Spartan-derived domains (right). (D) Confusion matrix between predicted clusters and anatomical labels. (E–F) Benchmarking against established methods (SDMBench). (E) Distributions of NMI, COM, HOM, and R using SDMBench-reported results. (F) Dataset-wise R score heatmap. (G–H) Benchmarking against recent methods. (G) Metric distributions for recently published methods evaluated in this study. (H) R score distributions across datasets.

datasets such as STARmap* and osmFISH, the cross-sample consensus step was omitted. Leiden clustering was applied to the aggregated graph corresponding to α_{best}, generating clustering assignments across a range of γ values. Evaluation metrics (ARI, NMI, HOM, COM) were reported as median values. For multi-sample datasets, Leiden clustering was applied to the aggregated graph for each sample using the corresponding α_{best}, producing clustering assignments across the same γ range. Median values of ARI, NMI, HOM, and COM were then computed for each sample.

The distribution of evaluation metrics (NMI, COM, HOM, and R) across datasets and methods is illustrated (Fig. 3E; Supplementary Figs. 10A, 11A, 12A). Both versions of Spartan (v1 and v2) show higher median performance across datasets, ranking within the top two methods in all datasets by R score. The relatively small interquartile range and higher upper quartile demonstrate Spartan's consistency and robustness across diverse datasets. This reduced variability suggests that the multiplex integration of LSA, neighborhood connectivity, and gene expression connectivity provides a more balanced and resilient representation of spatial domains. By contrast, all other methods exhibit wider interquartile ranges, reflecting greater dispersion in performance and sensitivity to dataset-specific features. Overall, Spartan not only achieves consistently high accuracy in identifying spatial domains but also delivers stable and reliable results across multi-sample datasets.

The R score heatmap across individual datasets (Fig. 3F; Supplementary Figs. 10B, 11B, 12B), further validates this observation. Spartan (both versions) consistently reaches the highest or near-highest scores, with particularly strong gains in complex imaging-based datasets like osmFISH and STARmap. These datasets are known for their irregular domain structures. Spartan's emphasis on LSA (via the **L** component) helps preserve domain continuity while still aligning with gene expression structure, explaining its robustness. The heatmap makes it evident that Spartan generalizes reliably across sequencing and imaging-based technologies equally well.

An aggregated view (Supplementary Fig. 1B) using a radar plot, highlighting trade-offs across evaluation metrics for all methods. Both versions of Spartan form the largest and most balanced profile, demonstrating consistently strong performance across all axes. In contrast, other methods often excel in one metric but underperform in others—for example, some graph-based approaches such as GraphST achieve reasonable completeness but sacrifice homogeneity. Spartan's multiplex framework, by integrating LSA, neighborhood connectivity, and gene expression connectivity, maintains both high completeness and homogeneity. This balanced performance is crucial in spatial transcriptomics, where capturing both global domain boundaries and local tissue coherence is necessary for biologically meaningful clustering.

Benchmarking against recently proposed methods

Here, three recently published methods for identifying spatial domains were implemented. These included SpatialLeiden [10], NichePCA [9], and BANKSY [8]. Two versions of SpatialLeiden were evaluated: SpatialLeiden (v1), which uses PCA for feature selection, and SpatialLeiden (v2), which employs MULTISPATI PCA [18] for feature selection. The KNN graph was used to encode the neighborhood connectivity of cells in both versions of the SpatialLeiden. The KNN configuration was demonstrated to perform better than Delaunay on imaging-based datasets in SpatialLeiden. NichePCA is a neighborhood-based spatial domain identification method that uses PCA on locally aggregated gene expression data to extract latent spatial features efficiently. BANKSY is a versatile method applicable to both sequencing-based and imaging-based technologies. Five datasets from the SDMBench (MERFISH, STARmap, STARmap*, BaristaSeq, osmFISH) were used to benchmark Spartan against these methods. In addition, the Vizgen MERFISH dataset was employed to assess Spartan's scalability and its ability to detect spatial domains in high-resolution samples.

The distribution of evaluation metrics (NMI, COM, HOM, and R) stratified by method, provides a per-method breakdown of performance consistency (Fig. 3G; Supplementary Figs. 13A-B, 14A-B, 15A-B, 16A-B). Both versions of Spartan maintain high central values with smaller interquartile ranges, underscoring their stability across datasets. In contrast, methods such as NichePCA, BANKSY, and SpatialLeiden exhibit wider spreads and greater variability. Importantly, Spartan performs well on both COM and HOM simultaneously, whereas competing methods often trade one for the other. This balanced performance reflects Spartan's multiplex design, which integrates LSA, and neighborhood structure to stabilize performance against dataset-specific challenges.

The R-score distributions across datasets are further examined and both versions of Spartan consistently rank among the top performers, with the strongest gains observed in complex datasets such as MERFISH and Vizgen MERFISH (Fig. 3H; Supplementary Figs. 13C, 14C, 15C, 16C). These datasets are characterized by fine-grained spatial heterogeneity between neighboring cells and non-uniform cell density. Spartan's incorporation of the LSA component allows it to capture these fine-scale differences by considering attribute deviations of spots or cells relative to their neighborhood. Additionally, Spartan's use of positional-randomness–agnostic graphs, such as the Delaunay graph, makes it particularly well-suited for these datasets, a feature that is especially evident in the Vizgen MERFISH results.

The R scores for two single-sample datasets (STARmap1k and osmFISH) are presented, offering a focused comparison across methods (Supplementary Figs. 1C, 15C). There is little difference in performance between methods, although once again, Spartan (both v1 and v2) achieves the highest or near-highest performance, underscoring its adaptability even when the dataset size is smaller. The fact that Spartan maintains high performance in both high-resolution, high fine-grained heterogeneity datasets (e.g., Vizgen MERFISH, Fig. 3H) and smaller single-sample datasets (Supplementary Fig. 1C) illustrates the method's scalability. This dual capability is crucial for practical applications, as spatial transcriptomics studies range from compact developmental tissues to large-scale brain or even whole organism atlases.

The ARI scores of Spartan (v1 and v2), NichePCA, SpatialLeiden (v1 and v2), and BANKSY across five datasets are shown in (Fig. 4A-B; Supplementary Fig. 2A-D). Regardless of version, Spartan achieves the highest ARI scores in three of five datasets (MERFISH, STARmap, and STARmap*), and ranks second in the remaining two (osmFISH and BaristaSeq). This demonstrates Spartan's accuracy in predicting spatial domains that align with the ground truth. It also underscores Spartan's versatility, performing consistently across both entropy-based metrics (NMI, HOM, COM, R) and pair-counting–based metrics such as ARI, highlighting its robustness across different evaluation frameworks.

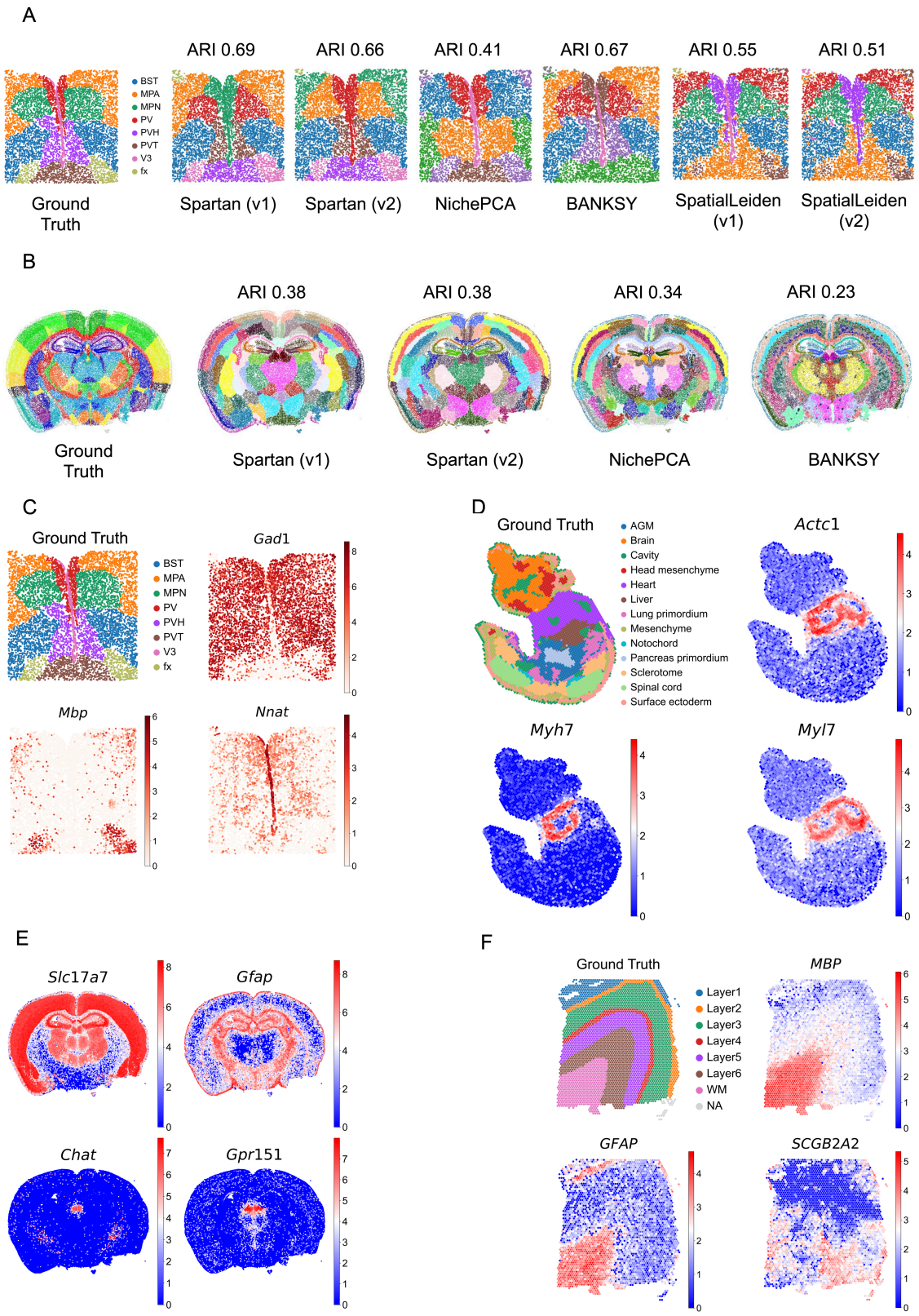

Figure 4. (A–B) Spatial domain identification for MERFISH 0.19 (SDMBench) and Vizgen MERFISH S2R3 samples. Ground-truth annotations (left) are compared with clustering results from Spartan (v1, v2), NichePCA, BANKSY, and SpatialLeiden (v1, v2). ARI values above each map quantify agreement with ground truth. (C) Spatially variable gene (SVG) examples for the MERFISH 0.19 sample. Spatial expression patterns align with anatomical boundaries and support the cluster assignments in (A). (D) Stereo-seq mouse embryo (E9.5E2S2). Ground-truth annotations (left) and spatial expression of representative embryo marker genes (right) show anatomically consistent localization. (E) SVGs for the Vizgen MERFISH mouse brain S2R3 sample, highlighting region- and cell-type–specific expression patterns. (F) 10x Visium human dorsolateral prefrontal cortex (DLPFC) sample 151673. Ground-truth cortical layers (left) and layer-enriched marker genes (right) demonstrate accurate laminar recovery.

Spatially variable gene identification using Spartan

We computed the Spatial Activation Quotient (SAQ) for all M genes using the weighted adjacency matrix $\mathbf{L}$, which represents the LSA graph of a given sample. The SAQ is formulated as a Rayleigh quotient [19], providing a measure of how strongly a gene's expression pattern aligns with the spatial structure encoded by $\mathbf{L}$. Genes with higher SAQ values exhibit stronger non-random spatial organization, indicating potential spatially variable genes (SVGs).

To assess the statistical significance of each gene's spatial activation, we performed spatial permutation testing. Specifically, we randomly permuted the spatial positions of spots, thereby destroying the original neighborhood structure while preserving each gene's expression distribution. For each permutation, SAQs were recomputed to generate a null distribution that reflects the range of SAQ values expected under spatial randomness.

The empirical p-value for each gene was then estimated as the proportion of permutations where the permuted SAQ exceeded (or equaled) the observed SAQ. This quantifies how unlikely a gene's spatial pattern is under the null hypothesis of no spatial structure. Finally, we applied False Discovery Rate (FDR) correction using the Benjamini–Hochberg procedure [20] to account for multiple hypothesis testing across all genes. The resulting FDR-adjusted p-values represent the global significance levels of spatial activation, with genes passing the threshold (FDR < 0.05) considered significantly spatially variable.

Spartan identifies cell-specific, layer-specific, and region-specific SVGs

In the preoptic and hypothalamic regions of the adult mouse brain sample, obtained from the MERFISH technology, Spartan effectively identifies spatially variable genes (SVGs) that delineate distinct anatomical and cellular domains (Fig. 4C; Supplementary Fig. 3A). The inhibitory neuron marker *Gad1* is detected across nearly all gray matter structures, including the bed nuclei of the stria terminalis (BST), medial preoptic area (MPA), medial preoptic nucleus (MPN), periventricular hypothalamic nucleus (PV), and paraventricular hypothalamic nucleus (PVH), but is absent in the fornix (fx) and paraventricular thalamic nucleus (PVT). This pattern accurately reflects the distribution of GABAergic neurons [21, 22], as the fx and PVT are primarily white matter and glutamatergic, respectively. Conversely, *Mbp* is strongly expressed only in the fx, highlighting oligodendrocyte-rich white matter tracts [23], whereas *Nnat* is restricted to the V3 ventricular zone, marking ependymal cells [24]. The calcium-regulatory gene *Sln* is present in most neuronal and ependymal regions [25] but absent in fx, and the neuropeptide gene *Oxt* is highly specific to the PVH, corresponding to magnocellular neurosecretory neurons [26]. Collectively, these SVGs reveal a coherent molecular anatomy, distinguishing inhibitory neurons, white matter, ependymal cells, and neuroendocrine centers.

In the Stereo-seq developing mouse embryo sample, Spartan captures region- and tissue-specific gene expression patterns that reflect early organogenesis (Fig. 4D; Supplementary Fig. 3B). Cardiac markers such as *Actc1*, *Myh7*, and *Myl7* are detected exclusively in the heart, with *Nppa* showing highly lateralized expression restricted to the left side of the heart, consistent with left–right patterning [27]. Hemoglobin genes (*Hba-a1*, *Hba-a2*) are expressed in the heart, liver, and fluid-filled cavity regions [28], including areas between the sclerotome and lung primordium, highlighting early erythropoietic activity. Other genes, such as *Gm42418*, are confined to cavity regions, while *Cdk8* and *Il31ra* are absent from specific tissues like the surface ectoderm, spinal cord, and brain regions, reflecting selective tissue differentiation. These findings demonstrate Spartan's ability to detect highly localized embryonic expression patterns that correspond to developmental biology [29, 30].

The Vizgen MERFISH mouse brain dataset further highlights Spartan's ability to capture regionally specialized neuronal and glial populations across the adult brain (Fig. 4E; Supplementary Fig. 3C). The excitatory neuron marker *Slc17a7* [31] is strongly expressed in the cerebral cortex, hippocampus, and thalamus, whereas the astrocytic marker *Gfap* is enriched in the hippocampal and hypothalamic regions. *Chat* and *Gpr151* [32] show selective expression in the medial and lateral habenula of the epithalamus, while *Gpr88* is enriched in the striatum of the cerebral nuclei, reflecting medium spiny neuron populations [33]. The muscarinic acetylcholine receptor *Chrm1* is present throughout the brain but with lower expression in the thalamus and hypothalamus, highlighting regionally modulated cholinergic signaling [34]. Collectively, these patterns capture both cortical and subcortical specialization, including excitatory, inhibitory, and modulatory neuronal circuits, as well as astrocytic distribution.

In the 10x Visium human dorsolateral prefrontal cortex (DLPFC) sample, Spartan identifies layer- and white matter-specific SVGs that recapitulate canonical cortical architecture (Fig. 4F; Supplementary Fig. 3D). *MBP* is highly expressed in the white matter (WM), marking oligodendrocyte populations [23], while *GFAP* is enriched in both WM and layer 1, highlighting astrocytic distribution [35] across superficial cortex and subcortical tracts. Layer-specific genes such as *COX6C* and *CST3* exhibit selective expression in combinations of deep and superficial layers (layers 1, 2, 5, and 6), whereas *FBXL16* is detected across all cortical layers except WM, indicating broad gray matter enrichment. *SCGB2A2*, although widely expressed, shows absence in portions of the left upper layers 1–4, reflecting subtle spatial heterogeneity. These findings indicate that Spartan accurately resolves both classical layer-specific markers and fine-scale lateralized expression patterns in the human cortex.

Across all four datasets, Spartan consistently identifies genes with high spatial specificity that correspond to known cell types, tissue structures, and functional domains. In the MERFISH mouse hypothalamus sample, the distinction between GABAergic nuclei, white matter tracts, and ependymal zones is clearly captured. In the Stereo-seq mouse embryo sample, tissue-specific expression reflects organogenesis and left–right patterning. In the 10x Visium human DLPFC sample, cortical layer specificity and white matter enrichment are resolved, while in the Vizgen MERFISH mouse brain dataset, regional specialization of neurons and astrocytes is detected across cortical, hippocampal, thalamic, and subcortical structures.

Notably, Spartan also captures subtle spatial heterogeneity and lateralization. Examples include *Nppa* restricted to the left heart, partial absence of *SCGB2A2* in upper cortical layers, and lateralized expression of *COX6C* in DLPFC layers. Such fine-scale detection demonstrates Spartan's sensitivity to both broad regional patterns and localized deviations.

Overall, Spartan's detection of spatially variable genes across multiple organs, and developmental stages demonstrates its robustness and biological fidelity. It accurately resolves

canonical markers, layer- and region-specific genes, and subtle spatial heterogeneities, making it a powerful platform for mapping molecular architecture in complex tissues.

Spartan preserves transferability of detected SVGs

Next, we evaluated Spartan's ability to preserve the transferability of spatially variable genes (SVGs). A gene identified as spatially variable in one SRT sample should exhibit a similar non-random spatial expression pattern in other samples from the same tissue type [15]. To test this, two different MERFISH samples representing the preoptic region of the mouse hypothalamus were used. The SVGs detected in one sample, *Nnat*, *Oxt*, *Gad1*, *Sln*, and *Mbp*, exhibited similar non-random spatial expression patterns in the other sample (Supplementary Fig. 4A-B). Importantly, SVGs that defined spatial domains in one sample also defined the same spatial domains in the other sample. For instance, *Mbp* showed high expression in the fx region in both samples, while *Sln* was restricted to the V3, MPN, BST, and PVT domains in both. Similarly, the presence of *Oxt* in the PVH region was preserved across samples. These results highlight Spartan's capability to identify authentic SVGs and accurately capture non-random spatial patterns.

Visium HD analysis: Spartan resolves anatomical layering and functional compartmentalization in the developing esophagus and stomach

To evaluate Spartan in a novel and biologically demanding setting, we applied it to an in-house high-resolution Visium HD section of the developing human esophagus and stomach at 10 weeks of gestation. This tissue comprises multiple epithelial cell types, concentric smooth muscle layers, heterogeneous stromal compartments, and vascular niches arranged along curved and continuous anatomical axes. The gastroesophageal junction (GEJ) represents a particularly challenging transitional region in which epithelial identity and stromal programs shift gradually rather than forming sharply demarcated boundaries. This structured resolution of a gradual transition zone suggests that activation-aware integration can partition gradual molecular gradients into spatially coherent domains.

Spartan resolved spatial domains across the entire specimen that aligned with known anatomical organization, including precise delineation of the GEJ (Fig. 5A). For this analysis, parameters were configured to emphasize the LSA component (**L**), enabling detection of spatially coherent transcriptional programs within fine-grained tissue heterogeneity. Multiple domains were supported by domain-restricted spatially variable genes (SVGs), whereas additional domains reflected anatomically meaningful microstructures captured through local transcriptomic sensitivity. Notably, Spartan identified the GEJ, outer muscularis layer, esophageal mesenchyme compartment, esophageal luminal epithelium, gastric mucosal epithelium, and three quantitatively stratified gastric stromal compartments characterized by graded enrichment of extracellular matrix, glycosaminoglycan, vascular, and immune-associated programs as coherent spatial domains. Compared to NichePCA (Fig. 5B), Spartan preserved anatomically consistent boundaries and spatial continuity along curved tissue structures, consistent with improved localization of domain-restricted programs in this tissue.

Spartan resolved the GEJ as domain 5 (Fig. 5A), defined by the presence of SVGs including *PLA2G2A*, gastric-associated mucins (*MUC5AC*, *MUC5B*), and squamous epithelial-associated markers such as the transcription regulator *ELF3*, and *TACSTD2* [36, 37] (Supplementary Fig. 17A-F). Co-expression of gastric-associated mucins alongside esophageal markers like *TACSTD2* supports a mixed transcriptional identity consistent with a junctional transition zone. Notably, however, *PLA2G2A* exhibited selective enrichment within this domain, whereas NichePCA distributed the signal across multiple adjacent partitions (Fig. 5A-B), further supporting the improved localization of regionally enriched programs by Spartan. *PLA2G2A* has been reported to function as an antimicrobial effector and modulator of gut microbiota, supporting epithelial barrier associated functions in the gastrointestinal tract [38]. Together, these findings suggest that activation-aware integration stabilizes partitions at transitional interfaces.

To further characterize spatial structure within the GEJ, we recursively applied Spartan within domain 5 to identify subdomains capturing localized transcriptional programs (Fig. 5C). Adjacent subdomains were differentiated using pairwise differential expression (DE) analysis, and discriminative marker sets were evaluated using logistic regression, yielding AUROC scores ranging from 0.703 to 0.945, indicating robust separability.

Subdomain 0 (Sub0) represented a secretory gastric epithelial-like compartment oriented towards the lumen, reflected by mucin-associated expression patterns (Supplementary Fig. 17B-C). Pairwise comparison against a left-side stromal subdomain (Sub3) yielded high discriminative performance (AUROC=0.945), consistent with distinct epithelial and collagen-rich stromal molecular states (Fig. 5D). On the right side of the GEJ, a remodeling-associated stromal compartment (Sub1) was distinguished by extracellular matrix reorganization programs (AUROC=0.915). Additional right-side subdomains captured deeper stromal niches with separable signaling and infrastructure associated transcriptional profiles (AUROC range 0.703–0.793)(Fig. 5D), illustrating Spartan's ability to resolve nested spatial microenvironments within a continuous transition zone. This analysis revealed pronounced asymmetry across the junction, with a coherent mucosal and stromal interface on the left side, and a multi-layered arrangement with distinct matrix remodeling and signaling associated compartments on the right side.

Beyond the GEJ, Spartan resolved the concentric multilaminar architecture of the fetal esophagus (Fig. 6A), identifying an outer muscularis layer (domain 0), an intermediate fibroblast-rich mesenchymal stroma (domain 3), and an inner luminal epithelium (domain 4) (Fig. 6B). In contrast, NichePCA grouped the luminal epithelium and intermediate stroma into a single domain. The muscularis externa (domain 0) formed a coherent contractile scaffold defined by smooth muscle associated SVGs, anchored by *TAGLN* [39] (Fig. 6B-D; Supplementary Fig. 18A-E). Quantitative analysis confirmed maximal enrichment within domain 0 and reduced enrichment at the GEJ, consistent with distinct molecular prioritization at the junction relative to surrounding muscle (Fig. 6C; Supplementary Fig. 18F). Domain 3 was supported by extracellular matrix associated stromal programs anchored by *FN1*, consistent with a fibroblast-rich supportive compartment (Fig. 6B-D; Supplementary Fig. 19). Domain 4 was supported by epithelial stratification associated expression patterns, including *KRT5*, a canonical basal epithelial marker in stratified epithelia [40] (Fig. 6B-D; Supplementary Fig. 20).

Spartan also identified the gastric mucosal epithelium (domain 2), characterized by a spatially coherent secretory program and epithelial identity (Fig. 6E). This compartment

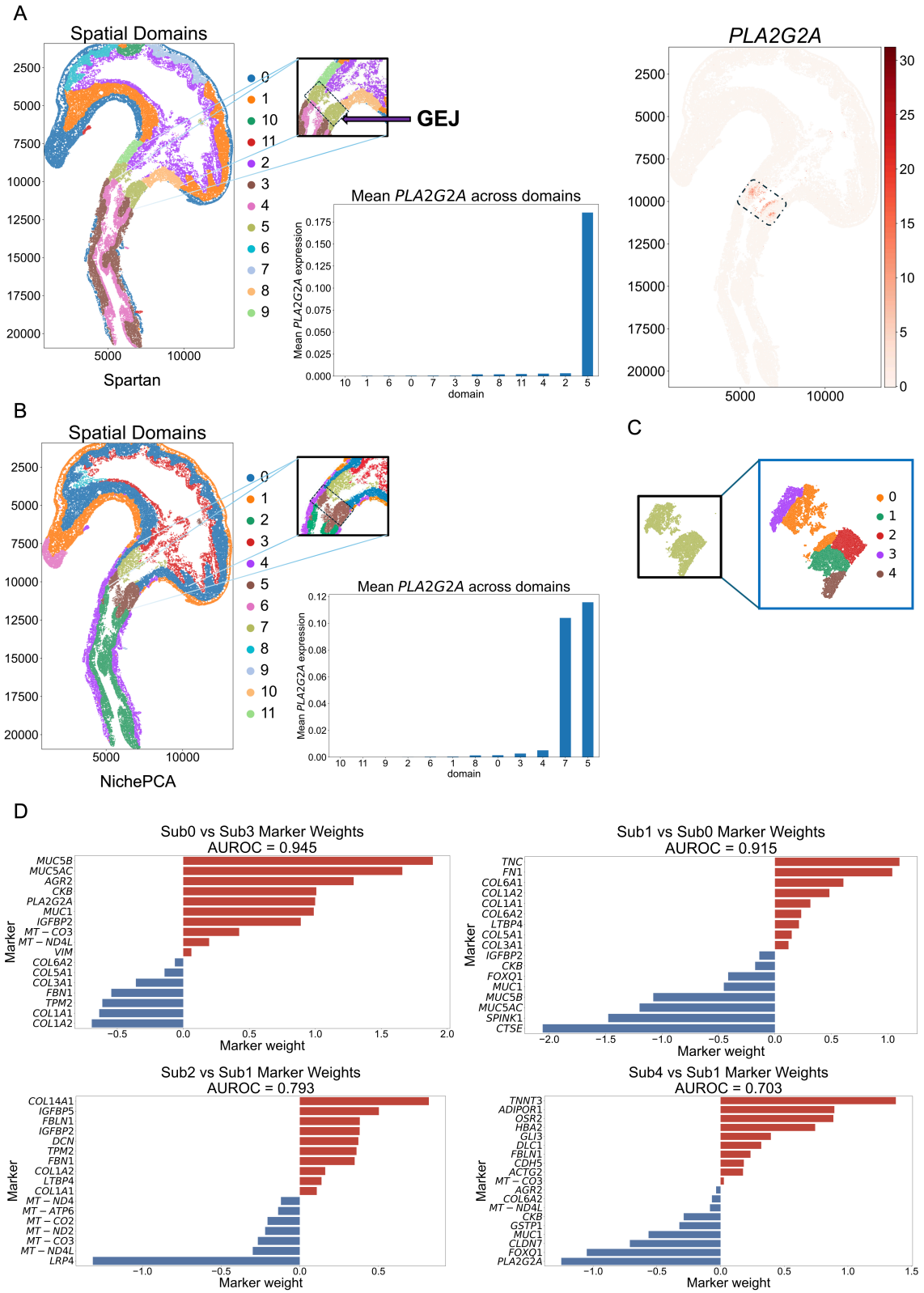

Figure 5. High-resolution domain reconstruction and GEJ subdomain stratification in Visium HD. (A–B) Spatial domains identified by Spartan (A) and NichePCA (B) on a Visium HD section of the developing human esophagus and stomach using 12 domains. Spartan preserves spatially coherent domains in anatomically complex regions, including the gastroesophageal junction (GEJ; Domain 5). Insets highlight the GEJ and spatial expression of *PLA2G2A*, with corresponding mean expression across domains. Domain colors are for visualization only and are not comparable across methods. (C–D) Supervised subdomain analysis within the GEJ. Subdomains were identified by reapplying Spartan to Domain 5 only. Marker weights correspond to logistic-regression coefficients from pairwise subdomain classification, and AUROC values (0.703–0.945) quantify subdomain separability.

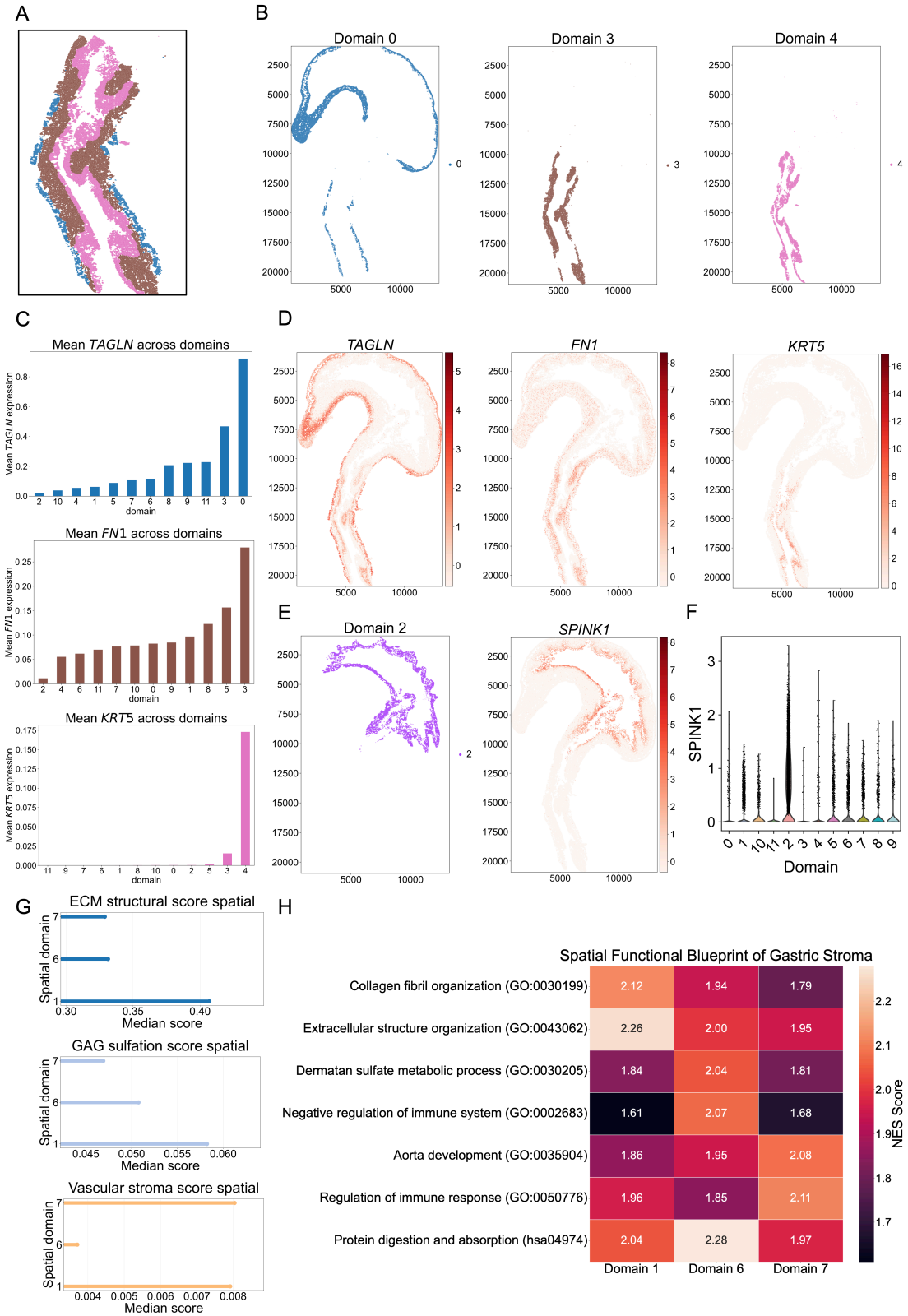

Figure 6. Reconstruction of esophageal laminar architecture and stromal functional programs using Visium HD. (A) Spartan resolves the concentric laminar organization of the developing esophageal wall, delineating epithelial, stromal and muscular compartments. (B) Spatial domains corresponding to outer muscularis (Domain 0), stromal interface (Domain 3), and luminal epithelium (Domain 4). (C) Mean expression of canonical markers across domains. *TAGLN* is enriched in Domain 0, *FN1* in Domain 3, and *KRT5* in Domain 4. (D) Spatial expression maps of *TAGLN*, *FN1*, and *KRT5* align with domain boundaries. (E) Gastric mucosal epithelium (Domain 2) with localized *SPINK1* expression. (F) Violin plot confirming *SPINK1* enrichment in Domain 2. (G) Median spatially smoothed module scores across stromal domains (Domains 1, 6, 7) reveal continuous functional gradients across adjacent compartments. (H) Gene set enrichment heatmap summarizing domain-associated programs: Domain 1 shows extracellular matrix enrichment, Domain 6 sulfated proteoglycan and immune-regulatory pathways, and Domain 7 vascular-associated signaling.

was supported by enrichment of a set of gastric epithelial marker genes including the gene encoding the mucosal protective protein *SPINK1* [41, 42] (Fig. 6E-F; Supplementary Fig. 21).

Surrounding this epithelium, Spartan resolved the gastric stroma into three specialized spatial domains, capturing regional heterogeneity that NichePCA grouped as a single domain. Domain 1 represents the structural framework of the gastric corpus, exhibiting the highest median extracellular matrix (ECM) and glycosaminoglycan (GAG) sulfation scores (Fig. 6G-H). Domain 6 represents the antral reservoir, showing peak enrichment for protein digestion and the dermatan sulfate metabolic process, while also contributing to immune regulation (Fig. 6G-H). Domain 7 is associated with deeper submucosal layers and is defined by programs linked to vascular development and immune response regulation (Fig. 6G-H).

Beyond coarse domain recovery, Spartan identifies localized stromal microstructures that provide a mechanistic justification for sub-compartmentalization. Domain 10, a spatially restricted niche embedded within gastric stroma, exhibits strong enrichment for erythroid-associated genes such as *SLC4A1* and *HBA2* (Supplementary Fig. 22A-D). The corresponding functional enrichment patterns highlight oxygen transport and heme-related biology (Supplementary Fig. 22E) supporting the interpretation that this region represents a blood-associated microenvironment rather than a generic fibroblast compartment. Stromal regions are frequently grouped into broad partitions by neighborhood-based approaches, whereas activation-aware integration enables separation of smaller but biologically coherent niches.

Similarly, the analysis of Domains 8 and 9 supports Spartan's ability to distinguish closely adjacent stromal subregions on either side of the lumen at the entrance to the stomach following the gastroesophageal junction (Supplementary Fig. 23A). While both domains belong to a broadly stromal context, their differential signatures suggest that they encode distinct microenvironments rather than noisy fragmentation (Supplementary Fig. 23B). Domain 8 shows strong enrichment of extracellular matrix-associated markers, including fibrillar collagens and matrix remodeling genes, exemplified by *FBLN1*, consistent with a structural stromal compartment (Supplementary Fig. 23B and Supplementary Fig. 23C). In contrast, Domain 9 is characterized by reduced levels of these markers but moderately enriched vascular-associated transcripts such as *PECAM1*, *CLDN5*, *PLVAP*, and *EGFL7*, supporting a vessel-associated stromal niche (Supplementary Fig. 23B and Supplementary Fig. 23D). Logistic regression based discrimination provides a quantitative measure of separability between these domains, further strengthening the argument that Spartan is resolving functional microstructure rather than producing arbitrary clusters (Supplementary Fig. S24). Together, these results demonstrate that Spartan can resolve spatially coherent anatomical layers and functionally distinct stromal compartments in a complex developing tissue.

Discussion and conclusion

Spatial transcriptomics is rapidly transitioning from coarse tissue maps to high-resolution profiling, where tens of thousands of spatial locations capture subtle biological structure along continuous anatomical axes. This shift exposes a computational limitation: many clustering approaches separate broad compartments but blur tissue boundaries, merge transitional zones, or miss localized microstructures that are biologically meaningful, particularly in developmental tissue where programs vary gradually yet change sharply at interfaces. Spartan is designed to address this challenge through an aggregated graph formulation that integrates spatial topology, Local Spatial Activation (LSA), an activation-aware component designed to amplify localized transcriptomic transitions that standard spatial or expression-only graphs may underrepresent, and gene expression connectivity.

Conceptually, LSA is grounded in spatial statistics, where local spatial autocorrelation metrics such as local Moran's I distinguish stable regions from transition zones. Within coherent domains, LSA values are low because each location is surrounded by transcriptionally consistent neighbors. At boundaries and microstructures, LSA increases as neighborhood composition changes locally. When integrated with gene expression connectivity, this activation-aware structure strengthens within-domain coherence while discouraging artificial smoothing across interfaces, enabling Leiden clustering to recover partitions with sharper anatomical alignment.

Spartan remains computationally practical as datasets increase in resolution and gene panel size (Supplementary Figs. 5–6). Runtime scales approximately linearly with the number of spatial locations, and high-resolution datasets such as Visium HD are processed within minutes on CPU. Efficiency derives from sparse local graphs and linear-time community detection, avoiding dense pairwise computations or model training. These properties position Spartan as a lightweight and scalable framework capable of accommodating future increases in spatial resolution without specialized hardware or extensive parameter tuning.

A practical advantage of Spartan is that it does not require ground-truth labels. Ground truth was used primarily for benchmarking and ablation studies. In unlabeled datasets, Spartan can be applied by varying the Leiden resolution to obtain partitions at the desired level of biological granularity. Optional stability-based pruning metrics may further constrain the search space but should be viewed as workflow guidance rather than definitive unsupervised proof of a universally optimal partition.

Spartan was designed for robustness to parameterization. Clustering performance varies smoothly across a broad range of multiplex weight allocations (β_1, β_2) without sharp optima (Supplementary Fig. 7), indicating that improvements are not driven by fragile tuning. For benchmarking, a single dataset-level α was selected using a cross-sample consensus procedure and subsequently fixed, avoiding per-sample optimization (Supplementary Figs. 8–9); performance remains stable across a wide α range. The smooth dependence on multiplex weights clarifies the role of LSA: its contribution can be increased without destabilizing clustering, which is particularly advantageous in high-resolution datasets with sharp spatial transitions, such as Visium HD and Vizgen MERFISH, where stronger activation improves boundary fidelity and local coherence. In this framework, LSA can act as a spatial transition detector, while complementary graph layers preserve global structural organization.

Spartan adopts practical defaults aligned with widely used standards across competing methods. The pipeline uses 30 principal components for PCA, a 10-nearest-neighbors graph for spatial topology, and a 15-nearest-neighbors graph for gene expression connectivity, consistent with defaults in NichePCA and SpatialLeiden. Delaunay triangulation is also supported, eliminating the need to specify a spatial neighborhood size and providing flexibility in irregular sampling layouts. These design

choices make Spartan reproducible and adaptable across SRT technologies.

We demonstrate Spartan's biological relevance using a cell-level Visium HD section of developing human esophagus and stomach at 10 weeks of gestation, containing layered smooth muscle, fibroblast-rich stroma, glandular epithelium, vascular niches, and the complex gastroesophageal junction (GEJ). Spartan resolves spatial domains across the specimen and separates the GEJ as a distinct transitional territory consistent with its mixed molecular identity. Recursive application within the GEJ reveals asymmetrically organized subdomains, supporting the interpretation that activation-aware graph integration enhances sensitivity to nested microenvironments in continuous tissue regions relative to expression-only or topology-only integration.

To assess robustness to clustering granularity, we varied the Leiden resolution for the Visium HD sample to obtain cluster counts spanning coarse to fine partitioning ($R = 7$–20) while fixing all other hyperparameters (Supplementary Figs. 25-26). Spartan exhibits stable behavior across this range. At low resolution ($R = 7$), it collapses into spatially contiguous macro-domains reflecting global tissue organization while preserving the GEJ as a coherent transition region. At higher resolution ($R = 16$–20), it introduces local subdomains through hierarchical refinement without disrupting anatomical continuity or fragmenting the GEJ. In contrast, NichePCA shows reduced anatomical alignment at low resolution and increasingly fragmented or stripe-like partitions at higher cluster counts.

Finally, Spartan extends beyond domain discovery to spatially variable gene detection. By leveraging activation-aware structure, Spartan identifies genes associated with localized transitions and domain-restricted programs, supporting interpretability and enabling mechanistic follow-up. Spartan therefore functions not only as a clustering method but also as a framework for understanding how spatial organization emerges from localized transcriptional programs.

In conclusion, Spartan introduces an activation-aware multiplex graph framework that integrates spatial topology, Local Spatial Activation, and gene expression connectivity. The method is robust to parameter variation while permitting adaptive weighting in high-resolution settings where microdomain boundaries are critical. By linking Local Spatial Activation to principles of local spatial autocorrelation in geostatistics, Spartan provides an interpretable and extensible framework for spatial systems-level analysis, with potential applications in cell–cell communication, developmental tissue remodeling, and spatial multi-omics integration.

Methods

Data preprocessing

Raw SRT data were processed following standard workflows described previously [43, 44]. Gene expression matrices were normalized to counts per cell and log-transformed using `Scanpy`'s *pp.normalize_total* function [43]. The resulting filtered expression matrix is denoted as $\mathbf{X} \in \mathbb{R}^{N \times M}$, where N represents the number of spots (or cells) and M the number of genes. For sequencing-based technologies such as 10x Visium, Visium HD, and Stereo-seq, highly variable genes (HVGs) were selected using `Scanpy`'s *pp.highly_variable_genes* functionality [43]. Throughout this work, each row $\mathbf{X}_i$ of $\mathbf{X}$ is referred to as a spot for simplicity, although the method is equally applicable when $\mathbf{X}_i$ represents a cell, for example in image-based assays such as MERFISH.

Principal component analysis (PCA) was applied to $\mathbf{X}$ to obtain a lower-dimensional feature representation $\mathbf{Y^{pca}} \in \mathbb{R}^{N \times P}$, where $P \ll M$ is the number of principal components. The feature matrix is represented as

$$\mathbf{Y^{pca}} = \begin{bmatrix} y^{pca}_{1,1} & y^{pca}_{1,2} & \cdots & y^{pca}_{1,P} \\ \vdots & \vdots & \ddots & \vdots \\ y^{pca}_{N,1} & y^{pca}_{N,2} & \cdots & y^{pca}_{N,P} \end{bmatrix}. \tag{1}$$

Equivalently, $\mathbf{Y^{pca}}$ can be expressed in terms of row vectors:

$$\mathbf{Y^{pca}} = \begin{bmatrix} \mathbf{y^{pca}_1} \\ \vdots \\ \mathbf{y^{pca}_N} \end{bmatrix}, \quad \mathbf{y^{pca}_i} \in \mathbb{R}^{1 \times P}. \tag{2}$$

In addition to standard workflows, Spartan has also been implemented in the `SpatialData` framework [45], leveraging its standardized data structures and interoperability features. SpatialData provides a FAIR-compliant (Findable, Accessible, Interoperable, and Reusable) framework for integrating and analyzing multimodal spatial omics data. Its design supports interoperability through a language-agnostic storage format, while a dedicated Python library enables unified access to diverse spatial data types. Datasets are represented through five core primitives, capturing different data modalities: Images (raster-based visual data), Labels (e.g., segmentation masks), Points (e.g., molecular detections), Shapes (e.g., polygons representing regions of interest or capture locations), and Tables (e.g., molecular counts and annotations). The format also maintains metadata for coordinate transformations and alignment procedures applied to individual datasets.

Spatial graph

The spatial graph is expressed as $gr^{\mathrm{s}} = (V_{\mathrm{s}}, E_{\mathrm{s}})$ where $V_{\mathrm{s}} = \{1, 2, \cdots, N\}$ and E_{s} is represented in the form of a binary adjacency matrix, $\mathbf{S} \in \mathbb{R}^{N \times N}$. We have used the `Squidpy` package [44] to construct graphs. Each element of the matrix $\mathbf{S}$, s_{ij}, represents:

$$s_{ij} = \begin{cases} 1, & \text{if } i \text{ and } j \text{ are neighbors based on spatial proximity} \\ 0, & \text{otherwise} \end{cases} \tag{3}$$

The spatial proximity is determined by constructing either: (i) a k-nearest neighbor (KNN) graph based on Euclidean distance in 2D space using spatial coordinates, where it finds k-nearest neighbors for each spot i. This results in a directed graph or undirected graph, depending on the type of coordinate system using `Squidpy`'s *coord_type* option: generic or grid, or (ii) a Delaunay graph where a spot i shares edges with spots that are treated as neighbors in the Delaunay triangulation of the spatial coordinates. This results in an undirected planar graph. The matrix $\mathbf{S}$ can be represented in terms of row vectors:

$$\mathbf{S} = \begin{bmatrix} \mathbf{s_1} \\ \vdots \\ \mathbf{s_N} \end{bmatrix}, \quad \mathbf{s_i} \in \mathbb{R}^{1 \times N} \tag{4}$$

Each vector $\mathbf{s_i} = (s_{i1}, \cdots, s_{iN})$ represents the spatial neighborhood of spot i where each s_{ij} is defined according to equation 3. The matrix $\mathbf{S}$ is stored as a sparse matrix for efficient memory usage and faster computation. Thus, the

neighbors of spot i might be fewer than N. In such cases, we store only K_i nonzero entries in $\mathbf{s_i}$ where K_i is the number of neighbors of spot i.

Row-normalized spatial weights matrix

The spatial weights matrix, $\mathbf{W} \in \mathbb{R}^{N\times N}$, is constructed where each element of the matrix w_{ij} represents the measure of spatial proximity between spot i and spot j. The spatial weight w_{ij} is calculated as:

$$w_{ij} = \frac{1}{d_{ij}} \cdot s_{ij} \tag{5}$$

where d_{ij} is the Euclidean distance between spot i and spot j. To ensure numerical stability, we add a small constant $\epsilon = 10^{-3}$ to d_{ij} in implementation, such that $w_{ij} = \frac{1}{d_{ij}+\epsilon} \cdot s_{ij}$. This value is typically several orders of magnitude smaller than typical inter-spot distances across all datasets analyzed and does not affect spatial weighting. The spatial weights matrix, $\mathbf{W}$, is then row-normalized so that each row of the matrix sums to 1. $\mathbf{W^r} = [w^r_{ij}]$ where $w^r_{ij} = \frac{w_{ij}}{\sum_j w_{ij}}$ is the final row-normalized spatial weights matrix. The matrix $\mathbf{W^r}$ is stored as a sparse matrix. We have used the `Squidpy` package to calculate the d_{ij} values. Thus, the $\mathbf{S}$ provides a binary connectivity structure based on raw spatial proximity, while the row-normalized weight matrix $\mathbf{W^r}$ refines this by accounting for distance. We use the row-normalized matrix $\mathbf{W^r}$ to construct the matrix $\mathbf{L}$ in the next section.

Local Spatial Activation (LSA) graph

The LSA graph is expressed as $gr^{\text{lsa}} = (V_{\text{lsa}}, E_{\text{lsa}})$ where $V_{\text{lsa}} = \{1, 2, \cdots, N\}$ and E_{lsa} is represented as the weighted adjacency matrix, $\mathbf{L} \in \mathbb{R}^{N\times N}$. $\mathbf{L}$ captures the neighborhood-weighted transcriptional transition strength between spatially adjacent spots. Each element, l_{ij}, gives the LSA value of spot i with respect to spot j.

We can divide the calculation of LSA of a spot i into three components:

Summary statistics of spot i

We calculate two summary statistics: the mean and variance of the neighborhood $\mathcal{N}_i$ of spot i. The neighborhood $\mathcal{N}_i$ consists of K_i neighbors of spot i where K_i is either the number of k-nearest neighbors of the spot i or the number of neighbors that share edges with the spot i in the Delaunay graph. The neighbors of spot i are determined from the matrix $\mathbf{S}$.

We calculate the mean feature vector of $\mathcal{N}_i$ as:

$$\mu_{\mathcal{N}_\text{i}} = \frac{\mathbf{y_i^{pca}} + \sum_{j=1}^{K_i} \mathbf{y_j^{pca}}}{K_i + 1}, \quad \mathbf{y_i^{pca}}, \mathbf{y_j^{pca}} \in \mathbf{Y^{pca}} \tag{6}$$

We calculate the local variance and the local variance norm of the neighborhood $\mathcal{N}_i$ as:

$${\sigma_{\mathcal{N}_\text{i}}}^2 = \frac{(\mathbf{y_i^{pca}} - \mu_{\mathcal{N}_\text{i}})^2 + \sum_{j=1}^{K_i} (\mathbf{y_j^{pca}} - \mu_{\mathcal{N}_\text{i}})^2}{K_i + 1} \tag{7}$$

$$\hat{\sigma_{\mathcal{N}_i}} = \|{\sigma_{\mathcal{N}_\text{i}}}^2\|_2 \tag{8}$$

where $\mathbf{y_i^{pca}}$ and $\mathbf{y_j^{pca}}$ are the feature vectors of spot i and spot j. The mean feature vector, $\mu_{\mathcal{N}_\text{i}} \in \mathbb{R}^P$, summarizes the transcriptional context of the surrounding tissue (neighborhood) and provides a smooth representation of the local expression trends. The local variance norm of the neighborhood $\mathcal{N}_i$, $\hat{\sigma_{\mathcal{N}_i}}$, is defined as the Euclidean norm ($\|\cdot\|_2$) of the neighborhood variance vector ${\sigma_{\mathcal{N}_\text{i}}}^2$. This ℓ_2 aggregation provides an isotropic summary of multivariate variance across principal components, preserving rotational invariance under orthogonal transformations in PCA space. Consequently, normalization is independent of arbitrary axis orientation while summarizing total latent variability within the neighborhood.

Attribute deviation

We measure the attribute deviation of spot i from its surroundings, $\mathcal{N}_i$:

$$\phi_i = \|(\mathbf{y_i^{pca}} - \mu_{\mathcal{N}_\text{i}})\|_2, \tag{9}$$

The quantity ϕ_i is the attribute deviation norm, measuring how much spot i deviates from its neighbors in PCA-reduced expression space. Lower values indicate low transcriptional deviation from the neighborhood mean while higher values indicate stronger deviation, in PCA-reduced expression space. Similarly, we calculate the attribute deviation of neighbor j of spot i, from $\mathcal{N}_i$ as:

$$\phi_j = \|(\mathbf{y_j^{pca}} - \mu_{\mathcal{N}_\text{i}})\|_2, \tag{10}$$

Note that ϕ_j is computed with respect to $\mu_{\mathcal{N}_\text{i}}$, making $\mathbf{L}$ asymmetric by construction.

Local Spatial Activation (LSA)

The LSA of spot i with respect to its neighboring spot j is defined as:

$$l_{ij} = \frac{\phi_i w^r_{ij} \phi_j}{\hat{\sigma_{\mathcal{N}_i}}}, \quad l_{ij} \geq 0 \tag{11}$$

Here, l_{ij}, consists of three components as shown in (Equation 11). The quantities ϕ_i and ϕ_j measure the magnitude of transcriptional deviation of spots i and j relative to the neighborhood of spot i. w^r_{ij} quantifies spatial proximity of spot i and spot j. The local variance norm $\hat{\sigma_{\mathcal{N}_i}}$ normalizes LSA values, ensuring scale invariance across spots in neighborhood $\mathcal{N}_i$. Exact zero neighborhood variance is theoretically possible but does not occur in practice in PCA-reduced expression space; therefore no additional regularization term is introduced in the denominator. l_{ij} takes a form similar to the local Moran's I, which is one of the Local Indicators of Spatial Association (LISA) in geostatistics [6]. However, l_{ij} quantifies the spatially weighted joint transcriptional deviation of spot i and spot j from the neighborhood of spot i, normalized by the local variance, within the graph gr^{lsa}. The adjacency matrix $\mathbf{L}$ of the LSA graph is an asymmetric weighted adjacency matrix and serves as one of the key components integrated into the aggregated graph (Equation 14), where it is balanced against global gene expression connectivity and raw spatial proximity.

Gene expression connectivity graph

We construct a gene expression connectivity graph in the form of a KNN graph in the PCA space, gr^{g}. The gr^{g} is expressed as $(V_{\text{g}}, E_{\text{g}})$ where $V_{\text{g}} = \{1, 2, \cdots, N\}$ and E_{g} is represented by the binary adjacency matrix, $\mathbf{G} \in \mathbb{R}^{N\times N}$. The gr^{g} encodes the neighborhood relationship between two spots based on their transcriptomic similarity. The similarity between spots i and j, ψ^g_{ij}, is measured as the Euclidean distance in PCA space (Equation 12), where smaller values correspond to higher transcriptomic similarity:

$$\psi^g_{ij} = \|\mathbf{y_i^{pca}} - \mathbf{y_j^{pca}}\|_2, \quad \mathbf{y_i^{pca}}, \mathbf{y_j^{pca}} \in \mathbf{Y^{pca}} \tag{12}$$

The adjacency matrix $\mathbf{G}$ encodes neighborhood connectivity. Each element of the adjacency matrix $\mathbf{G}$, gr^g_{ij} is defined as:

$$gr^g_{ij} = \begin{cases} 1, & \text{if } j \text{ is among the } k\text{-nearest neighbors of } i \\ 0, & \text{otherwise} \end{cases} \tag{13}$$

This adjacency matrix $\mathbf{G}$ forms the gene expression connectivity component of the aggregated graph (Equation 14), complementing LSA and raw spatial proximity.

Aggregated graph

The gr^{mul}, is an aggregated graph that combines three graphs gr^{s}, gr^{lsa}, and gr^{g}. The aggregated graph, gr^{mul}, is expressed as $(V_{\text{mul}}, E_{\text{mul}})$ where $V_{\text{mul}} = \{1, 2, \cdots, N\}$ and E_{mul} is represented as the weighted adjacency matrix $\mathbf{J} \in \mathbb{R}^{N \times N}$ and is formed as:

$$\mathbf{J} = (\alpha - \beta_1) \times \mathbf{L} + (1 - \alpha) \times \mathbf{G} + (\alpha - \beta_2) \times \mathbf{S} \tag{14}$$

where,

$$\begin{aligned} &\alpha \in [t_{min}, t_{max}], \quad \alpha, t_{min}, t_{max} \in \mathbb{R}_{>0} \\ &0 < t_{min} < t_{max} < 1 \\ &\beta_1 + \beta_2 = 0.5, \quad \beta_1, \beta_2 \leq \alpha \end{aligned} \tag{15}$$

In this formulation, the matrix $\mathbf{J}$ balances three complementary sources of structure: $\mathbf{L}$ that encodes LSA information of all spots, the gene expression connectivity matrix $\mathbf{G}$, and the raw spatial adjacency matrix $\mathbf{S}$. An entry j_{ij} of the matrix $\mathbf{J}$ is high when spot j belongs to the neighborhood $\mathcal{N}_i$ where $\mathcal{N}_i$ denotes the neighborhood of spot i and is supported either by high transcriptomic similarity or strong joint deviation relative to the neighborhood $\mathcal{N}_i$. The parameter α regulates the overall trade-off between spatial and expression-derived similarity. At the same time, the correction terms β_1 and β_2 ensure that the combined weight of the structural terms $\mathbf{L}$ and $\mathbf{S}$ evaluates to $2\alpha - 0.5$, which regulates their overall contribution and prevents the structural terms from overwhelming the expression-based connectivity term $\mathbf{G}$. We constrain the sum of the correction terms to $\beta_1 + \beta_2 = 0.5$ to ensure that the effective range sizes of all three parameters $(\alpha, \beta_1, \beta_2)$ are comparable. This constraint ensures that variation in α directly modulates the relative balance between structural ($\mathbf{L}$,$\mathbf{S}$) and transcriptomic ($\mathbf{G}$) components without altering their total structural contribution, thereby ensuring the identifiability of α. This yields a balanced integration of spatial and expression-derived information. Since $s_{ij}, gr^g_{ij} \in \{0, 1\}$ and $l_{ij} \geq 0$, it follows directly that $j_{ij} \geq 0$ for all i, j. Moreover, the non-negativity of the matrix $\mathbf{J}$ ensures compatibility with downstream analyses that require positive adjacency matrices, such as the Leiden algorithm.

Spatial biological partitioning

We use the Leiden clustering algorithm to partition the aggregated graph $gr^{\text{mul}} = (V_{\text{mul}}, E_{\text{mul}})$. We use the RBConfigurationVertexPartition quality function, $Q(\mathbf{J}, \gamma)$, that takes the weighted adjacency matrix $\mathbf{J}$ and a resolution parameter γ as inputs. It partitions V_{mul} into R non-overlapping clusters $\{C_1, C_2, \cdots, C_R\}$. The quality function $Q(\mathbf{J}, \gamma)$ maximizes the total edge weight within clusters relative to the null configuration. In this case, we refer to these clusters as spatial domains.

In practice, the resolution parameter γ controls the granularity of spatial domains. Together with the layer parameters $(\alpha - \beta_1, 1 - \alpha, \alpha - \beta_2)$, it can adapt to SRT datasets of varying sizes belonging to different technologies. This approach allows the algorithm to leverage the connectivity information encoded by $\mathbf{S}$ and $\mathbf{G}$, which provides neighborhood guidance, and the matrix $\mathbf{L}$, enriches the aggregated graph with activation-aware transition structure that is not captured by spatial proximity or expression connectivity alone. This formulation enables detection of spatial domains that reflect both neighborhood cohesion and activation at interfaces.

α-selection strategy

For our ablation and benchmarking study, we formulated a rigorous hierarchical α-selection strategy for determining the multiplex weighting parameter α of the matrix $\mathbf{J}$.

For a given multi-sample SRT dataset $D = \{\text{Sm}_1, \cdots, \text{Sm}_T\}$, where Sm_i denotes the ith sample and T is the total number of samples, the α-selection strategy consists of four stages:

1. **Range selection.** For each sample Sm_i in D, we defined the search ranges of the multiplex weighting parameter $\alpha \in [\alpha_l, \alpha_r]$ and the resolution parameter $\gamma \in [\gamma_l, \gamma_r]$. For every candidate $\alpha_i \in [\alpha_l, \alpha_r]$, we performed Leiden clustering across all γ values, yielding a set of clustering assignments $C^{\alpha_i} = \{C^{\alpha_i}_{\gamma_l}, \cdots, C^{\alpha_i}_{\gamma_r}\}$.
2. **Biological prior.** For benchmarking datasets with curated ground-truth, we pruned C^{α_i} to retain only those clustering assignments whose number of clusters matched the ground-truth domain count, forming $C^{(1)\alpha_i} \subset C^{\alpha_i}$. This constraint enforces biological realism and fair comparison. For each $C^{(1)\alpha_i}_j \in C^{(1)\alpha_i}$, we computed the evaluation metrics ARI, NMI, HOM, COM, and nLSAS.
3. **Spatial-stability prior.** We further refined $C^{(1)\alpha_i}$ by retaining only clustering assignments whose nLSAS values lay within the central stability band (40th–70th percentiles by default). This percentile-based filtering removes spatially fragmented partitions (low nLSAS) and over-smoothed, excessively merged partitions (high nLSAS), thereby selecting configurations that balance spatial coherence with domain resolution. The resulting pruned set $C^{(2)\alpha_i} \subset C^{(1)\alpha_i} \subset C^{\alpha_i}$ was used to compute the median of each evaluation metric across all $C^{(2)\alpha_i}_j \in C^{(2)\alpha_i}$.

   For each sample Sm_i, we thus obtained a collection of candidate α values and their corresponding median evaluation metrics, stored in a table $\mathcal{T}_{\text{Sm}_i}$, where each row represents one α_i and its associated metrics. Each table $\mathcal{T}_{\text{Sm}_i}$ was then sorted by median NMI in descending order, and only the top K candidates were retained to mitigate the influence of outliers (default K=50). The resulting table $\mathcal{T}'_{\text{Sm}_i}$ therefore contains only the most promising α configurations for that sample.

   Repeating Steps 1–3 for all samples in D yields a collection of tables $\mathcal{T} = \{\mathcal{T}'_{\text{Sm}_1}, \mathcal{T}'_{\text{Sm}_2}, \cdots, \mathcal{T}'_{\text{Sm}_T}\}$.
4. **Cross-sample consensus.** Let $\mathbb{S}_{\alpha_{\text{Sm}_i}}$ denote the set of α values contained in $\mathcal{T}'_{\text{Sm}_i} \in \mathcal{T}$. We computed the intersection of all such sets to obtain a consensus set of α values, $\mathbb{S}_{\alpha_{\text{cm}}}$, enforcing cross-sample generalizability by restricting selection to α values that were consistently high-performing across all samples (in our datasets the consensus intersection was non-empty). In cases where the consensus

intersection is empty, the union of top-K candidates is used with cross-sample averaging. For each $\alpha_{\mathrm{cm}_i} \in \mathbb{S}_{\alpha_{\mathrm{cm}}}$, we extracted its median evaluation metrics from all $\mathcal{T}'_{\mathrm{Sm}_i}$ tables and calculated the mean of the median NMI values across samples. The α_{cm_i} achieving the highest mean median NMI across the dataset was designated as α_{best}.

The resulting α_{best} represents a globally optimal and cross-sample generalizable weighting parameter for the matrix $\mathbf{J}$.

Parameter selection

Ablation study

The k value for the KNN graph was set to 10 for constructing the spatial graph and to 15 for constructing the gene expression connectivity graph. The parameter α, which balances spatial and transcriptomic contributions, was varied between 0.5 and 0.9. Two additional parameters, β_1 and β_2, controlled the relative weighting of the LSA and spatial neighborhood connectivity components; these were fixed at 0.26 and 0.24 (default setting), respectively, to emphasize spatial connectivity slightly more strongly. The resolution parameter γ for the Leiden algorithm was varied between 0.5 and 0.9. For all datasets, the number of ground truth clusters was provided as input for evaluation.

Benchmarking on SDMBench

The benchmarking parameters for Spartan were configured as follows. In feature selection and graph construction, the number of principal components (P) was fixed at 30 for all datasets. A total of 3,000 highly variable genes (HVGs) were selected, following [10], with HVGs required only for the Stereo-seq dataset. The k value for constructing the gr^s KNN graph was set to 10, and the gr^g KNN graph was constructed using 15 nearest neighbors. Except for the Stereo-seq dataset, the number of immediate neighbors was set to 4 and the ring size was set to 1.

For parameter tuning, the weight parameter α was bounded between 0.5 and 0.9 across datasets. The parameters β_1 and β_2 were fixed at 0.26 and 0.24, respectively. The resolution parameter γ was varied between 0.5 and 0.9 for most datasets but extended to the range [0.5, 1.2] for osmFISH and Stereo-seq. The thresholds v_l and v_h for nLSAS were fixed at 40 and 70 for all datasets, except for STARmap where they were fixed at 40 and 80.

Benchmarking against recently proposed methods

We used the same benchmarking pipeline for Spartan to evaluate its performance on five SDMBench datasets as discussed above. To evaluate NichePCA and BANKSY on SDMBench datasets, we adopted a similar benchmarking pipeline as detailed in [9]. Specifically, for each dataset, the number of nearest neighbors was varied between 5 and 20, and the value that performed well across all samples and all metrics within that dataset was selected. For SpatialLeiden, we chose their best-performing configuration, namely the configuration that uses a KNN graph to represent spatial connectivity. We adopted their technology-specific layer weight ratios as used in their SDMBench benchmarking.

For the Vizgen MERFISH dataset, we employed a different benchmarking workflow similar to that used in NichePCA. The grid-search strategy for identifying the optimal α was similar to Section Benchmarking on SDMBench, but here α was varied between 0.77 and 0.87. The parameters β_1 and β_2 were fixed at 0.20 and 0.30. Hence, we gave more emphasis to the structural terms, particularly the LSA component $\mathbf{L}$, compared to the expression-derived similarity component $\mathbf{G}$. After selecting the optimal α (i.e., α_{best}) from a representative sample, we ran the Leiden clustering algorithm on its aggregated graph. This α_{best} was then applied to all other samples, for which we reported the maximum values of ARI, NMI, HOM, and COM across the given set of clustering assignments. We adopted this strategy to align with the benchmarking approach used in NichePCA.

Spatial Activation Quotient

To identify genes with non-random spatial expression patterns (SVGs), we introduce the *Spatial Activation Quotient* (SAQ), denoted by $\mathbf{v^{saq}} \in \mathbb{R}^M$. This metric ranks genes according to the degree to which their expression profiles exhibit localized spatial structure rather than random variation.

We begin with the filtered gene expression matrix $\mathbf{X} \in \mathbb{R}^{N\times M}$, where N is the number of spots and M is the number of genes. Each gene vector is first column-wise mean-centered to remove global expression offsets:

$$\mathbf{X}^{'} = \mathbf{X} - \mu^{\mathbf{g}}, \quad \mu_j^g = \frac{1}{N}\sum_{i=1}^{N} X_{ij}, \quad j = 1, 2, \cdots, M \tag{16}$$

where $\mathbf{X}^{'} \in \mathbb{R}^{N\times M}$ is the mean-centered expression matrix and $\mu^{\mathbf{g}} \in \mathbb{R}^M$ is the gene-wise mean expression vector.

Next, we propagate the mean-centered expression through the LSA graph to obtain a smoothed version of the expression for each gene:

$$\mathbf{X^{sm}} = \mathbf{L}\mathbf{X}^{'}, \quad \mathbf{X^{sm}} \in \mathbb{R}^{N\times M} \tag{17}$$

Here, $\mathbf{L}$ is the weighted adjacency matrix of the LSA graph. The product $\mathbf{L}\mathbf{X}^{'}$ therefore represents a spatially weighted smoothing of expression values, such that each spot's value reflects its local neighborhood context. The LSA matrix $\mathbf{L}$ used for SAQ computation is constructed from PCA-reduced expression as described above and remains fixed during gene-level scoring.

We then quantify the alignment between the original expression profile of a gene and its spatially smoothed profile. For gene j, this is given by:

$$v_j^{sp} = \sum_{i=1}^{N} X_{ij}^{'} X_{ij}^{sm}, \quad j = 1, 2, \cdots, M \tag{18}$$

A large v_j^{sp} indicates that the expression pattern of gene j is highly consistent with its LSA-weighted spatially smoothed version, suggesting the presence of structured spatial organization.

To normalize for gene-specific variability and expression magnitude, we compute the squared ℓ_2 norm of each gene's mean-centered profile:

$$v_j^{norm} = \sum_{i=1}^{N} {X_{ij}^{'}}^2 = \|X_{*j}^{'}\|_2^2, \quad j = 1, 2, \cdots, M \tag{19}$$

Finally, the spatial activation quotient is defined as the ratio:

$$v_j^{saq} = \frac{v_j^{sp}}{v_j^{norm}}, \quad \mathbf{v^{saq}} \in \mathbb{R}^M \tag{20}$$

Intuitively, v_j^{saq} measures how strongly the expression of gene j aligns with its spatially smoothed pattern. Genes with

high SAQ values are those whose local fluctuations cannot be explained by random noise but instead reflect reproducible, non-random spatial structure. These genes are therefore strong candidates for spatially variable genes (SVGs) that define tissue organization and functional domains.

Evaluation metrics

To evaluate Spartan's performance on different SRT datasets and against representative and widely used methods for spatial domain identification. We have used the following metrics:

Adjusted Rand Index

The Adjusted Rand Index (ARI) measures the agreement between a predicted clustering and a ground truth partition while correcting for random label assignments. Given two clustering assignments: $U = \{U_1, U_2, \cdots, U_{\mathcal{R}}\}$ being the ground truth partition and $V = \{V_1, V_2, \cdots, V_{\mathcal{C}}\}$ being the predicted clustering of Spartan, of N spots. Let n_{ij} denote the number of spots simultaneously in cluster U_i and V_j.

Let $a_i = \sum_j n_{ij}$ and $b_j = \sum_i n_{ij}$ represent the cluster sizes in U and V respectively. The ARI is defined as:

$$\text{ARI} = \frac{\sum_{i,j}\binom{n_{ij}}{2} - \frac{\sum_i \binom{a_i}{2}\sum_j \binom{b_j}{2}}{\binom{N}{2}}}{\frac{1}{2}[\sum_i \binom{a_i}{2} + \sum_j \binom{b_j}{2}] - \frac{\sum_i \binom{a_i}{2}\sum_j \binom{b_j}{2}}{\binom{N}{2}}} \tag{21}$$

The numerator measures the excess agreement between the two clusterings relative to that expected by random chance, while the denominator normalizes the score so that random labelings yield an expected value of zero and identical clusterings yield a value of one. The ARI is invariant to label permutations and robust to differences in cluster sizes. In this work, we use the ARI as implemented in scikit-learn [46].

Normalized Mutual Information

The Normalized Mutual Information (NMI) quantifies the mutual dependence between a predicted clustering and a ground truth labeling. Given two clustering assignments: $U = \{U_1, U_2, \cdots, U_{\mathcal{R}}\}$ being the ground truth partition and $V = \{V_1, V_2, \cdots, V_{\mathcal{C}}\}$ being the predicted clustering of Spartan, of N spots.

Let $n_{ij} = |U_i \cap V_j|$, $a_i = \sum_j n_{ij}$ and $b_j = \sum_i n_{ij}$. Define the probability distributions $\mathcal{P}_U(i) = \frac{a_i}{N}$, $\mathcal{P}_V(j) = \frac{b_j}{N}$, and joint-probability $\mathcal{P}_{UV}(i,j) = \frac{n_{ij}}{N}$. The mutual information is:

$$MI(U,V) = \sum_{i,j} \mathcal{P}_{UV}(i,j) \log \frac{\mathcal{P}_{UV}(i,j)}{\mathcal{P}_U(i)\mathcal{P}_V(j)} \tag{22}$$

The entropies of the two clustering assignments are:

$$H(U) = -\sum_i \mathcal{P}_U(i) \log \mathcal{P}_U(i) \tag{23}$$

$$H(V) = -\sum_j \mathcal{P}_V(j) \log \mathcal{P}_V(j) \tag{24}$$

The NMI is defined as:

$$\text{NMI(U,V)} = \frac{MI(U,V)}{\frac{1}{2}(H(U) + H(V))} \tag{25}$$

The NMI(U,V) $\in$ [0,1]. A value of 1 indicates perfect agreement, and a value near 0 indicates essentially independent assignments. In our experiments, we compute NMI using scikit-learn [46].

Homogeneity and Completeness

Homogeneity (HOM) and Completeness (COM) are information-theoretic metrics that assess the quality of clustering with respect to known true cluster labels. Homogeneity (HOM) measures whether each predicted cluster contains only spots of a single ground truth cluster, while completeness assesses whether all spots of a given ground truth cluster are assigned to the same predicted cluster.

Formally, given ground truth labels $U = \{U_1, U_2, \cdots, U_{\mathcal{R}}\}$ and predicted clusters $V = \{V_1, V_2, \cdots, V_{\mathcal{C}}\}$, the conditional entropies are defined as:

$$H(U|V) = -\sum_{i,j} \frac{n_{ij}}{N} \log \frac{n_{ij}}{b_j} \tag{26}$$

$$H(V|U) = -\sum_{i,j} \frac{n_{ij}}{N} \log \frac{n_{ij}}{a_i} \tag{27}$$

where $n_{ij} = |U_i \cap V_j|$, $a_i = \sum_j n_{ij}$, $b_j = \sum_i n_{ij}$, and N is the total number of spots.

The entropy of true and predicted labels are $H(U) = -\sum_i \frac{a_i}{N} \log \frac{a_i}{N}$ and $H(V) = -\sum_j \frac{b_j}{N} \log \frac{b_j}{N}$. HOM and COM are then defined as:

$$\text{HOM} = 1 - \frac{H(U|V)}{H(U)} \tag{28}$$

$$\text{COM} = 1 - \frac{H(V|U)}{H(V)} \tag{29}$$

We compute both scores using scikit-learn's implementation [46].

R score

While individual clustering metrics such as NMI, homogeneity (HOM), and completeness (COM) each capture distinct aspects of clustering quality, they can vary in sensitivity depending on cluster purity or fragmentation. To obtain a balanced, single-value summary of clustering performance across these complementary information-theoretic measures, we define the R score [12] as their arithmetic mean:

$$\text{R} = \frac{\text{NMI} + \text{HOM} + \text{COM}}{3} \tag{30}$$

A higher R score indicates simultaneously high mutual information, cluster purity, and label completeness, thus providing a robust overall indicator of alignment between predicted and ground truth structures.

normalized Local Spatial Activation Score (nLSAS)

The normalized Local Spatial Activation Score (nLSAS) quantifies the degree of spatial coherence among spots belonging to the same cluster. It measures how strongly LSA values are concentrated within cluster boundaries, thereby reflecting the spatial compactness of the clustering solution.

Let $V = \{V_1, V_2, \cdots, V_{\mathcal{C}}\}$ denote the set of clusters, where $\mathcal{C}$ is the total number of clusters. For each spot $i \in \{1, 2, \cdots, N\}$, we define its LSA as:

$$L_i = \sum_{j=1}^{N} l_{ij}, \quad l_{ij} \in \mathbf{L} \tag{31}$$

where l_{ij} represents the LSA of spot i with respect to spot j, derived from the LSA matrix $\mathbf{L}$.

For each cluster $V_k \in V$, the mean LSA is computed as:

$$L_k^{\text{mean}} = \frac{\sum_{i \in V_k} L_i}{|V_k|}. \tag{32}$$

We then determine the maximum and minimum mean activation across all clusters:

$$L_{\max}^{\text{mean}} = \max_{k \in \{1,2,\cdots,\mathcal{C}\}} \{L_k^{\text{mean}}\}, \tag{33}$$

$$L_{\min}^{\text{mean}} = \min_{k \in \{1,2,\cdots,\mathcal{C}\}} \{L_k^{\text{mean}}\}. \tag{34}$$

To ensure comparability across clusters and datasets, we normalize the mean activations to the range $[0, 1]$ as:

$$\tilde{L}_k = \frac{L_k^{\text{mean}} - L_{\min}^{\text{mean}}}{L_{\max}^{\text{mean}} - L_{\min}^{\text{mean}} + 10^{-10}}, \tag{35}$$

where a small constant (10^{-10}) prevents numerical instability.

Finally, the normalized Local Spatial Activation Score (nLSAS) is defined as the average normalized activation across all clusters:

$$\text{nLSAS} = \frac{1}{\mathcal{C}} \sum_{k=1}^{\mathcal{C}} \tilde{L}_k. \tag{36}$$

nLSAS summarizes the distribution of LSA within cluster boundaries and provides a dataset-normalized proxy for spatial compactness. This metric provides an interpretable, dataset-normalized measure of how effectively a clustering algorithm (e.g., Spartan) captures spatially localized domains within the tissue.

Datasets

To assess Spartan's performance in spatial domain identification and spatially variable gene (SVG) detection, we have evaluated Spartan on a diverse group of SRT datasets, coming from many different technologies and tissue types. Seven of those datasets have been used for spatial domain identification and four of them for SVG detection. Across the manuscript, we use the term sample to describe a single slice or a tissue section of the SRT. We use dataset to describe a set of SRT samples. The description of each dataset are given below:

Stereo-seq

The Stereo-seq dataset is sequencing-based SRT dataset obtained by high-resolution technology that spans the full transcriptome. The dataset consists of nine samples from mouse embryo depicting organogenesis [11]. The samples of the dataset [47] have the following number of spots: 5,913 (E9.5E1S1), 5,292 (E9.5E2S1), 4,356 (E9.5E2S2), 5,059 (E9.5E2S3), 5,797 (E9.5E2S4), 18,408 (E10.5E1S1), 18,647 (E10.5E1S2), 18,670 (E10.5E1S3), and 8,494 (E10.5E2S1). The corresponding number of genes: 25,568 (E9.5E1S1), 23,756 (E9.5E2S1), 24,107 (E9.5E2S2), 24,238 (E9.5E2S3), 23,398 (E9.5E2S4), 25,201 (E10.5E1S1), 25,244 (E10.5E1S2), 25,647 (E10.5E1S3), and 22,385 (E10.5E2S1).

BaristaSeq

The BaristaSeq dataset is a SRT dataset obtained by barcoded BarisTaSeq technology [48] which allows faster image acquisition. The dataset [47] consists of three samples from the mouse primary cortex. The number of cells in the samples: 1,525 (Slice 1), 2,042 (Slice 2), and 1690 (Slice 3). The size of the gene panel is 79.

MERFISH

The MERFISH dataset is SRT dataset obtained from imaging-based MERFISH technology. The dataset represents the preoptic region of the mouse hypothalamus [49]. The dataset [47] consists of five samples with number of cells: 5,488 (Bregma-0.04), 5,557 (Bregma-0.09), 5,926 (Bregma-0.14), 5,803 (Bregma-0.19), and 5,543 (Bregma-0.24). The gene panel size is 155. The regional annotations of the dataset is published in [13].

osmFISH

The osmFISH dataset is an imaging-based SRT dataset obtained by nonbarcoded osmFISH technology [50]. The dataset [47] consists of one sample representing the mouse somatosensory cortex. The gene panel is made up of 33 marker genes. The sample consists of 4,839 cells. The regional annotations of the dataset is published in [51].

STARmap

The STARmap dataset is an imaging-based SRT dataset obtained by in-situ RNA-sequencing STARmap technology [52]. The dataset [47] consists of three samples from the high cognitive region of the brain, the medial prefrontal cortex. The samples consist of the following number of cells: 1,049 (BZ5), 1,053 (BZ9), and 1,088 (BZ14). The gene panel size is 166. All samples are annotated to four distinct layer structures [13].

*STARmap**

The STARmap* is imaging-based SRT dataset, version of the STARmap dataset but has 1020 genes. The dataset [47] consist of one sample with 1207 cells. The dataset represents the visual cortex with regions enriched with excitatory, non-neuronal, and inhibitory cell types, expertly annotated [52].

Vizgen MERFISH

The Vizgen MERFISH is imaging-based SRT dataset obtained by the MERFISH technology. The dataset contains a gene panel of 483 genes [53]. This includes canonical cell type markers, nonsensory G-protein coupled receptors (GPCRs), and Receptor Tyrosine Kinases (RTKs). Cell type markers are mapped using Vizgen's own pipeline. The dataset consists of four samples derived from the coronal section of the mouse brain. The number of cells in the samples are:78,329 (S1R1), 88884 (S1R2), 83,546 (S2R1), and 85,958 (S2R3). The samples are regionally annotated by [9].

10x Visium

The 10x Visium is spot sequencing-based SRT dataset. The dataset consists of 12 samples from the human dorsolateral pre-frontal cortex (DLPFC) region [54]. Each sample spans six neuronal layers and the white matter. The number of spots in the samples [47]: 4,226 (151507), 4,384 (151508), 4,789 (151509), 4,634 (151510), 3,661 (151669), 3,498 (151670), 4,110 (151671), 4,015 (151672), 3,639 (151673), 3,673 (151674), 3,592 (151675), and 3,460 (151676). The total number of genes in the dataset is 33,538. The dataset is expertly annotated with six neuronal layers and the white matter [55].

Visium HD dataset

High-resolution spatial transcriptomic profiling was conducted on a 10-week post-conception (wpc) human fetal gastroesophageal specimen using the Visium HD Spatial Gene Expression platform (10x Genomics). Developmental staging was

determined by foot length (8 mm) in combination with ultrasonographic assessment.

Human tissue collection and processing

Human embryonic material was obtained from elective terminations of pregnancy under ethical approval from the North West Research Ethics Committee (23/NW/0039), with written informed consent from participants and in accordance with the Human Tissue Authority Codes of Practice.

The esophagus, stomach, and proximal duodenum were dissected and fixed within 1 h post-collection in 4% paraformaldehyde under RNase-free conditions. Tissue was processed and paraffin-embedded using standard protocols. Sagittal sections (5 µm thickness) were obtained, with haematoxylin and eosin (H&E) staining performed on every eighth section for anatomical reference.

Sections selected for spatial transcriptomic profiling were processed following the Visium HD FFPE Tissue Preparation Handbook (CG000684) and the Visium HD Spatial Gene Expression Reagent Kits User Guide (CG000685). Sections were deparaffinised, destained, de-crosslinked, and permeabilised prior to overnight probe hybridisation. Following probe ligation and washing, probe transfer was performed using the 10x Genomics CytAssist instrument. Libraries were prepared using the Visium HD Spatial Gene Expression Reagent Kit according to the manufacturer's protocol and sequenced on an Illumina NovaSeq 6000 platform (SP flow cell, 100-cycle configuration).

Data preprocessing and cell-level binning

Raw sequencing data were processed using the Space Ranger pipeline (10x Genomics, version 3.1.2) with alignment to the GRCh38 reference genome (release 2020-A).

To achieve cell-level resolution, histological images were analysed using QuPath (version 0.5.1-arm64). Nuclei were detected based on intensity and morphological parameters derived from H&E staining, followed by watershed-based expansion of nuclear boundaries to approximate whole-cell areas. Segmentation parameters included intensity threshold of 0.1, background radius 5 µm, and a minimum cell area of 10 μm^2.

Custom cell-specific bins were generated by assigning Visium HD barcodes to segmented cell polygons based on centroid overlap between barcode spatial coordinates and cell boundaries. For each segmented cell, gene-wise UMI counts from overlapping barcodes were aggregated to generate a gene-by-cell count matrix.

Cells were filtered to retain those with $\geq$20 UMIs and a minimum cell area of 2000 μm^2.

The final preprocessed dataset comprised 84,732 segmented cells and 18,085 detected genes following quality control filtering.

Data availability

The authors analyzed eight publicly available and one in-house SRT datasets. The data were acquired from the following websites or accession numbers: (1) Stereo-seq, BaristaSeq, MERFISH, osmFISH, STARmap, STARmap*, 10x Visium datasets with regional annotations were downloaded from SDMBench; (2) Vizgen MERFISH dataset was downloaded from Vizgen MERFISH Mouse Brain Receptor Map; (3) The Visium HD dataset generated in this study is available in ArrayExpress under accession number E-MTAB-16671.

Code availability

An open-source implementation of the Spartan can be downloaded from Spartan GitHub repository.

Acknowledgments

The authors thank all the contributors of the public data which was used in this study. Muhammad Faiz was funded by BBSRC DTP award (BB/T008725/1).

References

1. Vivien Marx. Method of the year: spatially resolved transcriptomics. *Nature Methods*, 18(1):9–14, 2021.
2. Michaela Asp, Joseph Bergenstråhle, and Joakim Lundeberg. Spatially resolved transcriptomes—next generation tools for tissue exploration. *BioEssays*, 42(10):1900221, 2020.
3. Tsai-Ying Chen, Li You, Jose Angelito U Hardillo, and Miao-Ping Chien. Spatial transcriptomic technologies. *Cells*, 12(16):2042, August 2023.
4. Lukas Valihrach, Daniel Zucha, Pavel Abaffy, and Mikael Kubista. A practical guide to spatial transcriptomics. *Mol. Aspects Med.*, 97(101276):101276, June 2024.
5. P. A. P. Moran. Notes on continuous stochastic phenomena. *Biometrika*, 37(1-2):17–23, 1950.
6. Luc Anselin. Local indicators of spatial association—LISA. *Geogr. Anal.*, 27(2):93–115, April 1995.
7. V A Traag, L Waltman, and N J van Eck. From louvain to leiden: guaranteeing well-connected communities. *Sci. Rep.*, 9(1):5233, March 2019.
8. Vipul Singhal, Nigel Chou, Joseph Lee, Yifei Yue, Jinyue Liu, Wan Kee Chock, Li Lin, Yun-Ching Chang, Erica Mei Ling Teo, Jonathan Aow, Hwee Kuan Lee, Kok Hao Chen, and Shyam Prabhakar. BANKSY unifies cell typing and tissue domain segmentation for scalable spatial omics data analysis. *Nat. Genet.*, 56(3):431–441, March 2024.
9. Darius P Schaub, Behnam Yousefi, Nico Kaiser, Robin Khatri, Victor G Puelles, Christian F Krebs, Ulf Panzer, and Stefan Bonn. PCA-based spatial domain identification with state-of-the-art performance. *Bioinformatics*, 41(1), December 2024.
10. Niklas Müller-Bötticher, Shashwat Sahay, Roland Eils, and Naveed Ishaque. SpatialLeiden: spatially aware leiden clustering. *Genome Biol.*, 26(1):24, February 2025.
11. Ao Chen, Sha Liao, Mengnan Cheng, Kailong Ma, Liang Wu, Yiwei Lai, Xiaojie Qiu, Jin Yang, Jiangshan Xu, Shijie Hao, Xin Wang, Huifang Lu, Xi Chen, Xing Liu, Xin Huang, Zhao Li, Yan Hong, Yujia Jiang, Jian Peng, Shuai Liu, Mengzhe Shen, Chuanyu Liu, Quanshui Li, Yue Yuan, Xiaoyu Wei, Huiwen Zheng, Weimin Feng, Zhifeng Wang, Yang Liu, Zhaohui Wang, Yunzhi Yang, Haitao Xiang, Lei Han, Baoming Qin, Pengcheng Guo, Guangyao Lai, Pura Muñoz-Cánoves, Patrick H Maxwell, Jean Paul Thiery, Qing-Feng Wu, Fuxiang Zhao, Bichao Chen, Mei Li, Xi Dai, Shuai Wang, Haoyan Kuang, Junhou Hui, Liqun Wang, Ji-Feng Fei, Ou Wang, Xiaofeng Wei, Haorong Lu, Bo Wang, Shiping Liu, Ying Gu, Ming Ni, Wenwei Zhang, Feng Mu, Ye Yin, Huanming Yang, Michael Lisby, Richard J Cornall, Jan Mulder, Mathias Uhlén, Miguel A Esteban, Yuxiang Li, Longqi Liu, Xun Xu, and Jian Wang. Spatiotemporal transcriptomic atlas of mouse organogenesis using DNA nanoball-patterned arrays. *Cell*, 185(10):1777–1792.e21, May 2022.

12. Zhiyuan Yuan, Fangyuan Zhao, Senlin Lin, Yu Zhao, Jianhua Yao, Yan Cui, Xiao-Yong Zhang, and Yi Zhao. Benchmarking spatial clustering methods with spatially resolved transcriptomics data. *Nat. Methods*, 21(4):712–722, April 2024.
13. Zheng Li and Xiang Zhou. BASS: multi-scale and multi-sample analysis enables accurate cell type clustering and spatial domain detection in spatial transcriptomic studies. *Genome Biol.*, 23(1):168, August 2022.
14. Yahui Long, Kok Siong Ang, Mengwei Li, Kian Long Kelvin Chong, Raman Sethi, Chengwei Zhong, Hang Xu, Zhiwei Ong, Karishma Sachaphibulkij, Ao Chen, Li Zeng, Huazhu Fu, Min Wu, Lina Hsiu Kim Lim, Longqi Liu, and Jinmiao Chen. Spatially informed clustering, integration, and deconvolution of spatial transcriptomics with GraphST. *Nat. Commun.*, 14(1):1155, March 2023.
15. Jian Hu, Xiangjie Li, Kyle Coleman, Amelia Schroeder, Nan Ma, David J Irwin, Edward B Lee, Russell T Shinohara, and Mingyao Li. SpaGCN: Integrating gene expression, spatial location and histology to identify spatial domains and spatially variable genes by graph convolutional network. *Nat. Methods*, 18(11):1342–1351, November 2021.
16. Zixuan Cang, Xinyi Ning, Annika Nie, Min Xu, and Jing Zhang. Scan-it: Domain segmentation of spatial transcriptomics images by graph neural network. In *Proceedings of the 32nd British Machine Vision Conference (BMVC 2021)*, 2021. Paper1139.
17. Honglei Ren, Benjamin L Walker, Zixuan Cang, and Qing Nie. Identifying multicellular spatiotemporal organization of cells with SpaceFlow. *Nat. Commun.*, 13(1):4076, July 2022.
18. Stéphane Dray, Sonia Saïd, and Françis Débias. Spatial ordination of vegetation data using a generalization of wartenberg's multivariate spatial correlation. *J. Veg. Sci.*, 19(1):45–56, February 2008.
19. Roger A Horn and Charles R Johnson. *Matrix Analysis*. Cambridge University Press, Cambridge, England, June 2012.
20. Yoav Benjamini and Yosef Hochberg. Controlling the false discovery rate: A practical and powerful approach to multiple testing. *J. R. Stat. Soc. Series B Stat. Methodol.*, 57(1):289–300, January 1995.
21. Pauline Yahr. Sex difference and response to testosterone in gabaergic cells of the medial preoptic nucleus and ventral bed nuclei of the stria terminalis in gerbils. *Horm. Behav.*, 59(4):473–476, April 2011.
22. Mathias Uhlén, Linn Fagerberg, M. Hallström, Björn and others many˙ Gad1 – brain tissue expression (hypothalamus). The Human Protein Atlas, version 19, 2024. `https://v19.proteinatlas.org/ENSG00000128683GAD1/brain/Hypothalamus` (accessed 13 Nov. 2025).
23. Robert Gould and Scott Brady. Identifying mRNAs residing in myelinating oligodendrocyte processes as a basis for understanding internode autonomy. *Life (Basel)*, 13(4):945, April 2023.
24. Jessica L Braun, Mia S Geromella, Sophie I Hamstra, and Val A Fajardo. Neuronatin regulates whole-body metabolism: is thermogenesis involved? *FASEB Bioadv.*, 2(10):579–586, October 2020.
25. Nishadh Rathod, Jessi J Bak, Joseph O Primeau, M'lynn E Fisher, Lennane Michel Espinoza-Fonseca, Mary Joanne Lemieux, and Howard S Young. Nothing regular about the regulins: Distinct functional properties of SERCA transmembrane peptide regulatory subunits. *Int. J. Mol. Sci.*, 22(16):8891, August 2021.
26. Seoyoung Son, Steffy B Manjila, Kyra T Newmaster, Yuan-Ting Wu, Daniel J Vanselow, Matt Ciarletta, Todd E Anthony, Keith C Cheng, and Yongsoo Kim. Whole-brain wiring diagram of oxytocin system in adult mice. *J. Neurosci.*, 42(25):5021–5033, June 2022.
27. Nathaly Anto Michel, Senka Ljubojevic-Holzer, Heiko Bugger, and Andreas Zirlik. Cellular heterogeneity of the heart. *Front. Cardiovasc. Med.*, 9:868466, April 2022.
28. Deborah Hay, Jim R Hughes, Christian Babbs, James O J Davies, Bryony J Graham, Lars Hanssen, Mira T Kassouf, A Marieke Marieke Oudelaar, Jacqueline A Sharpe, Maria C Suciu, Jelena Telenius, Ruth Williams, Christina Rode, Pik-Shan Li, Len A Pennacchio, Jacqueline A Sloane-Stanley, Helena Ayyub, Sue Butler, Tatjana Sauka-Spengler, Richard J Gibbons, Andrew J H Smith, William G Wood, and Douglas R Higgs. Genetic dissection of the α-globin super-enhancer in vivo. *Nat. Genet.*, 48(8):895–903, August 2016.
29. Qingquan Zhang, Daniel Carlin, Fugui Zhu, Paola Cattaneo, Trey Ideker, Sylvia M Evans, Joshua Bloomekatz, and Neil C Chi. Unveiling complexity and multipotentiality of early heart fields. *Circ. Res.*, 129(4):474–487, August 2021.
30. Tianyi Sun, Alexander Grassam-Rowe, Zhaoli Pu, Yangpeng Li, Huiying Ren, Yanru An, Xinyu Guo, Wei Hu, Ying Liu, Yuqing Zheng, Zhu Liu, Kun Kou, Xianhong Ou, Tangting Chen, Xuehui Fan, Yangyang Liu, Shu Tu, Yu He, Yue Ren, Ao Chen, Zhouchun Shang, Zhidao Xia, Lucile Miquerol, Nicola Smart, Henggui Zhang, Xiaoqiu Tan, Weinian Shou, and Ming Lei. Dbh+ catecholaminergic cardiomyocytes contribute to the structure and function of the cardiac conduction system in murine heart. *Nat. Commun.*, 14(1):7801, November 2023.
31. Xianchao Du, Jiashuo Li, Minghui Li, Xinxin Yang, Zhipeng Qi, Bin Xu, Wei Liu, Zhaofa Xu, and Yu Deng. Research progress on the role of type I vesicular glutamate transporter (VGLUT1) in nervous system diseases. *Cell Biosci.*, 10(1):26, March 2020.
32. Beatriz Antolin-Fontes, Kun Li, Jessica L Ables, Michael H Riad, Andreas Görlich, Maya Williams, Cuidong Wang, Sylvia M Lipford, Maria Dao, Jianxi Liu, Henrik Molina, Nathaniel Heintz, Paul J Kenny, and Ines Ibañez-Tallon. The habenular g-protein-coupled receptor 151 regulates synaptic plasticity and nicotine intake. *Proc. Natl. Acad. Sci. U. S. A.*, 117(10):5502–5509, March 2020.
33. Renaud Massart, Jean-Philippe Guilloux, Virginie Mignon, Pierre Sokoloff, and Jorge Diaz. Striatal GPR88 expression is confined to the whole projection neuron population and is regulated by dopaminergic and glutamatergic afferents. *Eur. J. Neurosci.*, 30(3):397–414, August 2009.
34. Mohammad Golam Sabbir. Cholinergic receptor muscarinic 1 co-localized with mitochondria in cultured dorsal root ganglion neurons, and its deletion disrupted mitochondrial ultrastructure in peripheral neurons: Implications in alzheimer's disease. *J. Alzheimers. Dis.*, 98(1):247–264, 2024.
35. Shelley L Forrest, Jordan Hanxi Kim, Daniel R Crockford, Katharine Huynh, Rosie Cheong, Samantha Knott, Madison A Kane, Lars M Ittner, Glenda M Halliday, and Jillian J Kril. Distribution patterns of astrocyte populations in the human cortex. *Neurochem. Res.*, 48(4):1222–1232, April 2023.
36. F Wang, X Liu, P Yang, L Guo, C Liu, H Li, S Long, Y Shen, and H Wan. Loss of TACSTD2 contributed to

squamous cell carcinoma progression through attenuating TAp63-dependent apoptosis. *Cell Death Dis.*, 5(3):e1133, March 2014.

37. The Human Protein Atlas. The human protein atlas: TACSTD2 expression in esophagus, 2026.
38. Yoshitaka Taketomi, Yoshimi Miki, and Makoto Murakami. Old but new: Group IIA phospholipase A2 as a modulator of gut microbiota. *Metabolites*, 12(4):352, April 2022.
39. Kiyomi Tsuji-Tamura, Saori Morino-Koga, Shingo Suzuki, and Minetaro Ogawa. TAGLN, a canonical marker of smooth muscle cells, is present in endothelial cells and involved in angiogenesis. *J. Cell Sci.*, 134(15), July 2021.
40. Hongming Huang, Kai Sen Tan, Suizi Zhou, Tian Yuan, Jing Liu, Hsiao Hui Ong, Qianmin Chen, Junxiao Gao, Minghong Xu, Zhenchao Zhu, Qianhui Qiu, and De Yun Wang. p63+krt5+ basal cells are increased in the squamous metaplastic epithelium of patients with radiation-induced chronic rhinosinusitis. *Radiat. Oncol.*, 15(1):222, September 2020.
41. The Human Protein Atlas. The human protein atlas: SPINK1 expression in stomach, 2026.
42. Yong H. Sheng, Garrett Z. Ng, Kim M. Summers, Alison L. Every, Gareth Price, Sumaira Z. Hasnain, Philip Sutton, and Michael A. McGuckin. Influence of the muc1 cell surface mucin on gastric mucosal gene expression profiles in response to helicobacter pylori infection in mice. *Frontiers in Cellular and Infection Microbiology*, Volume 10 - 2020, 2020.
43. F Alexander Wolf, Philipp Angerer, and Fabian J Theis. SCANPY: large-scale single-cell gene expression data analysis. *Genome Biol.*, 19(1), December 2018.
44. Giovanni Palla, Hannah Spitzer, Michal Klein, David Fischer, Anna Christina Schaar, Louis Benedikt Kuemmerle, Sergei Rybakov, Ignacio L Ibarra, Olle Holmberg, Isaac Virshup, Mohammad Lotfollahi, Sabrina Richter, and Fabian J Theis. Squidpy: a scalable framework for spatial omics analysis. *Nat. Methods*, 19(2):171–178, February 2022.
45. Luca Marconato, Giovanni Palla, Kevin A Yamauchi, Isaac Virshup, Elyas Heidari, Tim Treis, Wouter-Michiel Vierdag, Marcella Toth, Sonja Stockhaus, Rahul B Shrestha, Benjamin Rombaut, Lotte Pollaris, Laurens Lehner, Harald Vöhringer, Ilia Kats, Yvan Saeys, Sinem K Saka, Wolfgang Huber, Moritz Gerstung, Josh Moore, Fabian J Theis, and Oliver Stegle. SpatialData: an open and universal data framework for spatial omics. *Nat. Methods*, 22(1):58–62, January 2025.
46. Fabian Pedregosa, Gaël Varoquaux, Alexandre Gramfort, Vincent Michel, Bertrand Thirion, Olivier Grisel, Mathieu Blondel, Peter Prettenhofer, Ron Weiss, Vincent Dubourg, Jake Vanderplas, Alexandre Passos, David Cournapeau, Matthieu Brucher, Michaël Perrot, and Édouard Duchesnay. Scikit-learn: Machine learning in Python. *Journal of Machine Learning Research*, 12:2825–2830, 2011.
47. Zhiyuan Yuan, Fangyuan Zhao, Senlin Lin, Yu Zhao, Jianhua Yao, Yan Cui, Xiao-Yong Zhang, and Yi Zhao. Sdmbench: A spatial domain benchmark for spatial transcriptomics data. `http://sdmbench.drai.cn/`, 2024. Accessed: 2025-11-13.
48. Xiaoyin Chen, Yu-Chi Sun, George M Church, Je Hyuk Lee, and Anthony M Zador. Efficient in situ barcode sequencing using padlock probe-based BaristaSeq. *Nucleic Acids Res.*, 46(4):e22–e22, February 2018.
49. Jeffrey R Moffitt, Dhananjay Bambah-Mukku, Stephen W Eichhorn, Eric Vaughn, Karthik Shekhar, Julio D Perez, Nimrod D Rubinstein, Junjie Hao, Aviv Regev, Catherine Dulac, and Xiaowei Zhuang. Molecular, spatial, and functional single-cell profiling of the hypothalamic preoptic region. *Science*, 362(6416):eaau5324, November 2018.
50. Simone Codeluppi, Lars E Borm, Amit Zeisel, Gioele La Manno, Josina A van Lunteren, Camilla I Svensson, and Sten Linnarsson. Spatial organization of the somatosensory cortex revealed by osmFISH. *Nat. Methods*, 15(11):932–935, November 2018.
51. Simone Codeluppi et al. Data and code availability: Expression data (loom file) with osmfish data. `http://linnarssonlab.org/osmFISH/availability/`, 2018. Linnarsson Lab, Accessed: 2025-11-13.
52. Xiao Wang, William E Allen, Matthew A Wright, Emily L Sylwestrak, Nikolay Samusik, Sam Vesuna, Kathryn Evans, Cindy Liu, Charu Ramakrishnan, Jia Liu, Garry P Nolan, Felice-Alessio Bava, and Karl Deisseroth. Three-dimensional intact-tissue sequencing of single-cell transcriptional states. *Science*, 361(6400):eaat5691, July 2018.
53. Inc. Vizgen. Merfish mouse brain receptor map — mouse brain map dataset. `https://info.vizgen.com/mouse-brain-map?submissionGuid=a66ccb7f-87cf-4c55-83b9-5a2b6c0c12b9`, 2025. Accessed: 2025-11-13.
54. Kristen R Maynard, Leonardo Collado-Torres, Lukas M Weber, Cedric Uytingco, Brianna K Barry, Stephen R Williams, Joseph L Catallini, 2nd, Matthew N Tran, Zachary Besich, Madhavi Tippani, Jennifer Chew, Yifeng Yin, Joel E Kleinman, Thomas M Hyde, Nikhil Rao, Stephanie C Hicks, Keri Martinowich, and Andrew E Jaffe. Transcriptome-scale spatial gene expression in the human dorsolateral prefrontal cortex. *Nat. Neurosci.*, 24(3):425–436, March 2021.
55. KristenR. Maynard, Leonardo Collado-Torres, LukasM. Weber, Cedric Uytingco, BriannaK. Barry, StephenR. Williams, JosephL. II Catallini, MatthewN. Tran, Zachary Besich, Madhavi Tippani, Jennifer Chew, Yifeng Yin, JoelE. Kleinman, ThomasM. Hyde, Nikhil Rao, StephanieC. Hicks, Keri Martinowich, and AndrewE. Jaffe. Spatial transcriptomics data (10×visium) for the human dorsolateral prefrontal cortex hosted in spatiallibd. `http://research.libd.org/spatialLIBD/`, 2021. Accessed: 2025-11-13.